

A probe of the maximum energetics of fast radio bursts through a prolific repeating source

O. S. Ould-Boukattine^{◇,1,2}, P. Chawla^{1,2}, J. W. T. Hessels^{2,1,3,4}, A. J. Cooper⁵,
M. P. Gawroński⁶, W. Herrmann⁷, F. Kirsten^{8,1}, D. M. Hewitt², D. C. Konijn^{9,1},
K. Nimmo¹⁰, Z. Pleunis^{2,1}, W. Puchalska⁶, M. P. Snelders^{1,2}

◇ ouldboukattine@astron.nl

¹ *ASTRON, Netherlands Institute for Radio Astronomy, Oude Hoogeveensedijk 4, 7991 PD Dwingeloo, The Netherlands*

² *Anton Pannekoek Institute for Astronomy, University of Amsterdam, Science Park 904, 1098 XH Amsterdam, The Netherlands*

³ *Trottier Space Institute, McGill University, 3550 rue University, Montréal, QC H3A 2A7, Canada*

⁴ *Department of Physics, McGill University, 3600 rue University, Montréal, QC H3A 2T8, Canada*

⁵ *Astrophysics, The University of Oxford, Keble Road, Oxford, OX1 3RH, UK*

⁶ *Institute of Astronomy, Faculty of Physics, Astronomy and Informatics, Nicolaus Copernicus University, Grudziadzka 5, 87-100 Toruń, Poland*

⁷ *Astroteiler Stockert e.V., Astroteiler 1-4, 53902 Bad Münstereifel, Germany*

⁸ *Department of Space, Earth and Environment, Chalmers University of Technology, Onsala Space Observatory, 439 92, Onsala, Sweden*

⁹ *Kapteyn Astronomical Institute, University of Groningen, Kapteynborg 5419, 9747 AD, Groningen, The Netherlands*

¹⁰ *MIT Kavli Institute for Astrophysics and Space Research, Massachusetts Institute of Technology, 77 Massachusetts Ave, Cambridge, MA 02139, USA*

Abstract

Fast radio bursts (FRBs) are sufficiently energetic to be detectable from luminosity distances up to at least seven billion parsecs (redshift $z > 1$). Probing the maximum energies and luminosities of FRBs constrains their emission mechanism and cosmological population. Here we investigate the maximum energetics of a highly active repeater, FRB 20220912A, using 1,500 h of observations. We detect 130 high-energy bursts and find a break in the burst energy distribution, with a flattening of the power-law slope at higher energy. This is consistent with the behaviour of another highly active repeater, FRB 20201124A. Furthermore, we model the rate of the highest-energy bursts and find a turnover at a characteristic spectral energy density of $E_v^{\text{char}} = 2.09_{-1.04}^{+3.78} \times 10^{32}$ erg/Hz. This characteristic maximum energy agrees well with observations of apparently one-off FRBs, suggesting a common physical mechanism for their emission. The extreme burst energies push radiation and source models to their limit.

Introduction

Fast radio bursts¹ (FRBs) are observed with durations ranging from microseconds² to seconds³ and fluences ranging from about 0.01 Jy ms to 1000 Jy ms^{4,5}. Of the thousands of known FRBs, most are observed as one-off events and only a few percent are known to repeat⁶. It remains unclear whether the repeaters and apparent non-repeaters have different astrophysical origins. An exceptionally bright (MJy) burst has been observed from the Galactic magnetar SGR 1935+2154, and strongly suggests that at least some FRBs originate from magnetars^{7,8}.

Though FRB emission is almost certainly beamed, the beaming fraction is unknown. For simplicity, isotropic-equivalent energies are used to compare different FRBs even though this is an overestimation of the total energy released in radio waves. Given the typical Mpc- to Gpc-distances of FRBs⁹, their isotropic-equivalent energies are known to range from roughly $E = 10^{37} - 10^{42}$ erg. This is at least four orders-of-magnitude larger than what is measured for Galactic radio pulsars, including the giant pulses seen from the Crab pulsar¹⁰. SGR 1935+2154, however, is known to produce bursts whose energies span the range between pulsars and FRBs (Ref. ¹¹ and references therein).

Furthermore, it is expected that the detected radio energy is only a small fraction ($\sim 10^{-5}$) of the total bolometric energy released at the source during an FRB event^{12,13}. Taking this into account, the most energetic known FRBs may be associated with $\sim 10^{46-47}$ erg events that are comparable to the most extreme ‘giant flares’ from magnetars¹⁴, though still at least four orders-of-magnitude less energetic compared to supernovae and gamma-ray bursts. Nonetheless, FRBs display extreme brightness temperatures $T_B \gg 10^{12}$ K (the typically assumed threshold between incoherent and coherent emitters), and therefore must originate from a coherent emission process². This makes them detectable across cosmic distances despite their relatively modest energetics compared to other extreme astrophysical phenomena.

The distribution of observed FRB spectral energies (E_ν) follow a differential power law, where the rate above some spectral energy scales as $R(> E_\nu) \propto E_\nu^{\gamma_D}$ for a differential index γ_D . For the overall population of apparently non-repeating sources^{15,16}, $\gamma_D \sim -1.5$. Highly active repeating FRBs provide the opportunity to measure the burst energy distribution of a single source. In the case of repeaters, the energy distribution has been shown to deviate from a simple power law^{5,17}.

The most energetic FRBs are also by far the most rare. Therefore, large on-sky time is essential to probe the extremes of the FRB population. By probing the maximum energetics of FRBs, we can constrain the emission mechanism^{18,19}; the total cosmic population^{15,16,20}; and inform how best to detect FRBs with upcoming telescopes.

There are various conceivable ways to investigate the maximum achievable energies and luminosities of FRBs, including 1. discovery of exceptionally distant or energetic one-off bursts²¹; 2. population modelling of the full observed sample of FRBs^{15,16}; and 3. high-cadence monitoring of hyperactive repeating sources^{5,22} (those repeaters that are sometimes seen to produce hundreds of bursts per hour, if observed with a high-sensitivity radio telescope). These methods complement each other, given that they are all subject to different observational biases and challenges. Moreover, it remains unclear whether apparently one-off and repeating FRBs share the same progenitors and emission mechanisms. By ‘progenitor’, we mean the type of astrophysical source powering the bursts, and by ‘emission mechanism’ we mean the physical process that generates the bursts. Probing the maximum observed energies of repeaters and apparently one-off FRBs is thus also a way to compare their nature.

In this work we investigate the maximum burst energy and luminosity of FRB 20220912A, using multiple 25-32 m-class radio telescopes that together provide unprecedented observational coverage in terms of on-sky time. FRB 20220912A was discovered using the CHIME/FRB system²³, and was soon identified as a hyperactive source compared to most other known repeaters. It was localised to a host galaxy at $z = 0.0771$ ^{24,25}

and has been the target of many follow-up observations. The exceptionally high activity of FRB 20220912A makes it an ideal source to map the burst energy distribution of a repeater. Here we specifically focus on the maximum achievable burst energy and luminosity.

Observations, analysis and results

We observed FRB 20220912A using four European radio telescopes: the Westerbork RT-1 25-m in the Netherlands (Wb); the Onsala 25-m in Sweden (O8); the Stockert 25-m in Germany (St); and the Toruń 32-m in Poland (Tr). These observations span 117 days between MJD 59867 and 59983 (15 October 2022 until 08 February 2023) for a total of 2192 hours, which reduces to 1491 hours of unique on-source time when taking into account the overlap between different observing modes and telescopes. During our campaign we observed at P-band (330 MHz), L-band (1.4 GHz), and C-band (4.7 GHz) with the aim of observing simultaneously over a wide bandwidth, as much as possible. Table 1 gives an overview of the different observing setups. Our data recording and burst searching strategy match that of earlier work⁵. At Wb, Tr and O8 we recorded amplitude and phase data (raw voltages) and at St we recorded total intensity data (Methods). We searched for bursts using standard methods adapted to the specifics of each telescope (Methods).

We detected 130 bursts from FRB 20220912A. Of these, 114 unique bursts were detected at 1.4 GHz, including 16 bursts that were detected by multiple telescopes simultaneously. Remarkably, the highest-energy bursts from FRB 20220912A contributed to $22.0^{+15.6}_{-10.3}$ % of the all-sky rate of FRBs at L-band ($\mathcal{F} > 500$ Jy ms; Methods). We also detected 16 unique bursts at 330 MHz, while no bursts were detected at 4.7 GHz. Although we sometimes had simultaneous coverage between all observing bands, see Extended Data Figure 1, we did not detect any burst at multiple frequency bands. Each burst is labeled with an ID, Bx, numbered in order of their arrival time, and followed by the telescope code to

indicate which instrument detected the burst (e.g., B15-Tr). A subset of bursts, preferentially those with high S/N, is shown in Figure 1; a complete overview of all the bursts can be found in the Supplementary Material.

We used a single dispersion measure (DM) of $219.375 \text{ pc cm}^{-3}$ for all bursts detected at L-band in order to correct for the dispersive delay²⁵. For bursts detected at P-band, which mostly occurred at a different time range, we determined the best-fit DM to be $219.735 \text{ pc cm}^{-3}$ (Methods and Extended Data Figure 3). We determined the time of arrival (ToA), fluences, energetics, width, and frequency extent for each burst (Methods and Supplementary Table 2). We used incoherently dedispersed data to determine these properties, with the exception of the ToAs for bursts detected by Wb and Tr where we used coherently dedispersed data (Methods). Due to the high S/N and strong scintillation of the bursts, we encountered instrumental saturation effects. Therefore, we applied a similar method as in a previous work, where we correct for this effect to accurately determine the fluences and energetics⁵ (Extended Data Figure 2; Methods).

In addition to the new data we present here, our analysis also makes use of three additional observational campaigns towards FRB 20220912A, which were performed during the same time range: 8.67 h of observations with the Five-hundred-meter Aperture Spherical Telescope (FAST)²⁶; 61 h of observations with the Nançay Radio Telescope (NRT)²⁷; and 541 h of observations with the Allen Telescope Array (ATA)²².

In Figure 2 we show the cumulative burst energy distribution, denoted with slope γ_C , for detections from Westerbork, Stockert, FAST and NRT at L-band (1.4 GHz) — between MJD 59869 (17 October 2022) and MJD 59910 (27 November 2022). Constraining the time period allows us to directly compare the determined slopes for the different observational campaigns, while avoiding the potential pitfall of a burst energy distribution that evolves with time. For the high-energy bursts ($E_\nu > 3 \times 10^{30}$ erg/Hz) detected by Stockert we find a power-law index of $\gamma_C^{\text{st}} = -0.99 \pm 0.02 \pm 0.06$ and for Westerbork

we find $\gamma_C^{\text{Wb}} = -0.74 \pm 0.05 \pm 0.08$ (Methods). For the low-energy bursts ($E_\nu < 3 \times 10^{30}$ erg/Hz) from FAST we find a significantly steeper slope of $\gamma_C^{\text{FAST}} = -1.84 \pm 0.03 \pm 0.13$ (Methods). The burst energy distribution of NRT is best fit by a broken power law, see Extended Data Figure 4, where we find a break-point at $E_{\text{break}} \sim 3.2 \times 10^{30}$ erg/Hz. The power law below this break-point follows a steep slope $\gamma_C^{\text{NRT-1}} = -1.69 \pm 0.01 \pm 0.05$ and above this break-point it is flatter $\gamma_C^{\text{NRT-2}} = -0.60 \pm 0.08 \pm 0.05$ (Methods). Figure 2 shows the cumulative distribution for the bursts detected at P-band (330 MHz) by Westerbork, where we find a best-fit power law with index $\gamma_C^{\text{Wb}} = -1.10 \pm 0.07 \pm 0.15$.

Combining the burst detections from Wb, Tr, St, NRT, ATA, and FAST above the completeness threshold of our least sensitive telescope (Wb), we then model this combined data set with a Schechter function because we expect a physical limit to FRB energies and this description allows for direct comparison with previous modelling of one-off FRBs (Table 2; Methods). We find a characteristic maximum energy of $E_\nu^{\text{char}} = 2.09_{-1.04}^{+3.78} \times 10^{32}$ (erg/Hz) with a differential power law index of $\gamma_D = -1.12_{-0.13}^{+0.17}$ (Supplementary Table 2; Methods). In Figure 3 we show the differential distribution of burst energies over-plotted with a Schechter function using the median values of the posterior distributions from the MCMC run. We also indicate the determined characteristic maximum energy and uncertainty range.

We find that FRB 20220912A produced sufficiently bright bursts that optical telescopes have the required sensitivity to detect a fiducial optical afterglow of shock-based FRB models with prompt (<hour) follow-up (Extended Data Figure 5; Methods). Additionally, we also show that the brightest burst would have been detectable even if the source was at redshift $z = 9.9_{-1.1}^{+1.1}$, assuming that high-energy bursts are emitted at higher radio frequencies (Methods). These high-energy bursts, emitted at high redshift, could potentially be observed by future telescopes with good field-of-view (FoV) and increased sensitivity, such as CHORD²⁸. Upcoming radio telescopes with extremely large FoV but lower sensi-

tivity, such as BURSTT (FoV $\sim 10^4$ deg²)²⁹, will accumulate a large number of observing hours on repeating sources like FRB 20220912A and probe the high-energy burst distribution. Furthermore, these events could also be detected in the far side lobes of CHIME/FRB³⁰.

Discussion

Activity of hyperactive repeaters

We find that the burst energy distribution of FRB 20220912A can not be described by a single power law. Rather, it is well described by a broken power law ($E_\nu^{\text{break}} \sim 3.2 \times 10^{30}$ erg/Hz) and an exponential cut-off ($E_\nu^{\text{char}} = 2.09_{-1.04}^{+3.78} \times 10^{32}$ erg/Hz). The burst energy distribution is steeper ($\gamma_C^{\text{NRT-1}} = -1.69 \pm 0.01 \pm 0.05$) below the break, and flatter ($\gamma_C^{\text{NRT-2}} = -0.60 \pm 0.08 \pm 0.05$) above it. Previous work also showed that another hyperactive repeater, FRB 20201124A, has a similar break in its energy distribution at ($E_\nu^{\text{break}} \sim 8 \times 10^{30}$ erg/Hz) as well as a similar flattening: from $\gamma_C^{\text{FAST}} = -1.95 \pm 0.001 \pm 0.06$ at lower energies to $\gamma_C^{\text{O8+St}} = -0.48 \pm 0.11 \pm 0.03$ at the highest burst energies⁵. The occurrence of a break requires explanation; it could indicate two populations of bursts produced by distinct physical mechanisms⁵. The similarity in the break point energy between FRB 20220912A and FRB 20201124A suggests that this is a common feature that may be observed in the future for other repeaters.

For FRB 20201124A, mapping the energy distribution required comparing high-energy bursts from high-cadence observations with 25-32 m-class telescopes⁵ with lower-energy burst detections from FAST³¹. For FRB 20220912A we follow the same approach, comparing our detections to the lower-energy bursts observed by FAST²⁶. Additionally, we are able to detect the break in the power law burst energy distribution using NRT data alone²⁷ because NRT has good sensitivity and ample exposure time during the most intense period of activity (Figures 2 and 4; in comparison, the smaller dishes have a lower apparent rate because they missed the highest activity window

around MJD 59879). The NRT distribution initially follows the slope of FAST, but then breaks and flattens towards higher energies following the slope of St and Wb. The observation of a break in the distribution by a single instrument is unprecedented; it underlines and confirms the flattening of the energy distribution towards higher energies.

The ATA observed FRB 20220912A for 541 h and fit a power law to the cumulative distribution of burst energies²². They find a slope of $\gamma_C^{\text{ATA}} = -1.08_{-0.25}^{+0.25}$. The energy range we are able to probe in this work overlaps with the ATA and allows for direct comparison. We find that the slopes for different instruments beyond the break point in the distribution, see Figure 2, are consistent within uncertainties between all telescopes.

The telescopes used in this work (St, Wb, Tr, and O8) all have observing bandwidths ranging between 56 – 256 MHz, which is considerably narrower compared with the ATA (672 MHz) and NRT (512 MHz). Comparing the results of the cumulative power-law indices between all telescopes in the high-energy range shows comparable results, which indicates that the flattening in the distribution towards higher energies can not simply be accounted for by the limited bandwidth of observation.

We observed 14 bursts at P-band above our completion threshold, see Figure 2. Based on our sample we are unable to shed light on whether the cumulative energy distribution breaks at the same energy compared to L-band and if the differential distribution turns over at a similar characteristic energy. To further investigate the presence of a break-point at low radio frequencies, requires a higher-sensitivity observational campaign capable of probing bursts in the lower-energy regime ($E_\nu < 10^{30}$ erg/Hz).

Characteristic maximum energy

Determining the characteristic maximum spectral energies of FRBs is crucial to constrain their emission mechanisms and nature. For FRB 20220912A we find $E_\nu^{\text{char}} = 2.09_{-1.04}^{+3.78} \times 10^{32}$ erg/Hz or, equivalently, a total energy

$\log_{10}(E^{\text{char}}) = 41.32_{-0.30}^{+0.45}$ erg, assuming a 1-GHz emission bandwidth (Figure 3). Our findings agree with the inferred fluence limit $\mathcal{F} \lesssim 10^4$ Jy ms²² (or, equivalently, $\log_{10}(E^{\text{char}}) = 42.15$ erg) for FRB 20220912A to be consistent with the all-sky fluence distribution extrapolated from ASKAP Fly’s Eye survey³².

Previously, constraints on E^{char} have been derived from population studies of apparently one-off FRBs. In these cases, the energy distribution is modelled as a Schechter function. Two of these studies²⁰ combined data from various surveys including UTMOST, HTRU and CRAFT, with another study only using the FRBs in the first CHIME/FRB catalog¹⁶. The detection of an FRB at $z = 1.016$ with an implied burst energy of $6.4 \pm 0.7 \times 10^{41}$ erg also enabled a strong constraint on the characteristic maximum energy¹⁵. From these various studies, E^{char} ranges between $\log_{10}(E^{\text{char}}) = 41.26 - 42.08$ erg (Table 2). Our determined value of E^{char} for FRB 20220912A is consistent with the different population studies of apparently one-off FRBs.

For the slope of the differential distribution, we find $\gamma_D = -1.12_{-0.13}^{+0.17}$, which agrees with previous studies though the uncertainties on the measured slopes are large (Table 2). In our fitting of a Schechter function, we have only considered bursts above the completeness threshold of the least sensitive telescope (Wb) and with $E_\nu^{\text{char}} > 3.3 \times 10^{32}$ erg/Hz, to avoid bursts that follow a steeper power-law index below this value (Figure 2). We note that previous population studies may be including low-energy bursts that follow a different energy distribution, and which would skew the power-law slope of a Schechter fit to be apparently steeper.

During our burst search, we set the detection threshold at $S/N > 7$ (Methods). However, in our previous work⁵, we adopted a conservative approach and assumed a S/N of 15 as our completeness threshold. In this work, we test the dependence of the characteristic maximum energy on the adopted completeness threshold by varying the assumed S/N . Varying the threshold involves modelling of the Schechter function with different total number of bursts, see Supplementary Ta-

ble 1. The completeness thresholds are referenced with respect to the completeness of the least sensitive telescope (Wb). For a threshold of 10σ , the reduced chi-square implies a poor fit, which can be explained by our sample of detections from the 25–32-m telescopes being incomplete at that threshold. Adopting higher detection thresholds of 20– and 30σ results in $\chi^2 < 1$, which indicates overfitting of the data. Placing the completeness threshold exactly at the breakpoint (E_{break}) of the distribution gave results consistent with those for a 15σ threshold, suggesting that this threshold appropriately characterises our observations.

To test whether a Schechter function is preferred over a simpler power-law function, we fit both models and compute the Bayesian information criterion (BIC) which is defined as,

$$\text{BIC} = k \ln(n) - 2 \ln(\hat{L}) \quad (1)$$

Where k is the number of parameters, n the number of data points and \hat{L} the maximised value of the likelihood function from the MCMC run. The number of data points is in both models taken as the number of bins ($n = 20$); the number of parameters is $k = 2$ for the power-law function and $k = 3$ for the Schechter function. Since we make use of flat priors, we take the sample with the highest probability as the maximum likelihood sample, which is $\ln(\hat{L}) = -41.64$ for the power-law function and $\ln(\hat{L}) = -33.53$ for the Schechter function. This results in BIC values of 89.26 for the power-law function and 76.05 for the Schechter function. A BIC difference of 13.21 indicates that the fitting of the Schechter function is a more appropriate description of the data.

Constraining the FRB emission mechanism

Extremely bright FRBs are valuable for constraining the progenitors and emission mechanisms of FRBs. To examine these constraints, we consider the most energetic bursts observed at L-band and P-band: B68-Wb and B128-Wb, respectively. These bursts have measured energies of 2.8×10^{40} erg and 2.0×10^{40} erg, respectively, determined by multiplying the observed spectral energy density with the bandwidth of each burst. To

be more conservative, this calculation differs from previous calculations where we use a canonical adopted bandwidth of 1 GHz to convert to burst energies. As such, these values can be considered as lower limits on the isotropic-equivalent burst energy.

For typical radio efficiencies assumed in ‘far-away’ FRB models¹² of $\epsilon_{\text{radio}} \approx 10^{-5}$, these bursts require extreme event energies $E_{\text{flare}} > 10^{45}$ erg, consistent with magnetar giant flares. Magnetospheric ‘close-in’ FRB models often invoke crustal dislocations as the mechanism by which particle acceleration is triggered. Given an event energy, a required magnetic field can be derived assuming fiducial crustal oscillation parameters³³. If $\epsilon_{\text{radio}} \approx 10^{-5}$, an FRB with $E_{\text{FRB}} = 2 \times 10^{40}$ erg implies a local field strength $B \approx 2 \times 10^{16}$ G, suggesting that B68-Wb/B128-Wb require very large magnetic fields, plausibly stemming from multipolar field components or extreme crustal dislocations.

Coherent curvature radiation (CCR) by bunches has been discussed as a radiation mechanism for generating magnetospheric FRBs^{34,35}. There is a maximum peak luminosity of CCR based on an upper limit to the electric field E_{\parallel} , above which Schwinger pairs rapidly screen the field³⁶. The requirement that the momenta of radiating particles remains well-aligned also implies a maximal bunch luminosity¹⁹.

To characterise the limit of these constraints on the source of FRB 20220912A, we consider the burst in our sample with the highest peak luminosity (S_{ν}): B77-St. We calculate the luminosity as³⁷,

$$L_{\nu} = \frac{S_{\nu} \cdot 4\pi D_L^2}{(1+z)^{1+\alpha}} \quad (2)$$

Where S_{ν} is the peak flux density, $4\pi D_L^2$ the distance luminosity factor and $(1+z)^{1+\alpha}$ the redshift correction. resulting in a peak spectral luminosity of $L_{\nu, \text{B77-st}} = 1.38 \times 10^{35}$ erg s⁻¹ Hz⁻¹, measured at a time resolution of $\Delta t = 218.45$ μ s. In Figure 4, we show the minimum local magnetic field of the emission region based on the aforementioned maximum luminosities. These limits set conservative constraints on the surface magnetic field (e.g., corresponding to emission directly from the

surface). Therefore, if B77-St is powered by CCR along open field lines, it must stem from a region with $B \gtrsim 10^{12}$ G.

Source energy reservoir constraints

Assuming a perfect dipolar magnetic field, the total external magnetospheric energy reservoir of a neutron star can be crudely estimated as:

$$U_B \approx \frac{R_{\text{NS}}^3 B_s^2}{8\pi} \approx 4 \times 10^{46} \text{ erg} \left(\frac{R_{\text{NS}}}{10^6 \text{ cm}} \right) \left(\frac{B_s}{10^{15} \text{ G}} \right)^2 \quad (3)$$

Here, B_s is the surface magnetic field and R_{NS} is the neutron star radius. To examine the total energetics we integrate over the best fit differential burst energy distribution function (Figure 3). The total radio energy of bursts observed across the 1769 unique observing hours of all observing campaigns at L-band included in the dataset (assuming minimal overlap) above $E_{\text{radio, min}} = 3.3 \times 10^{30} \text{ erg Hz}^{-1}$ is: $1.3 \times 10^{42} \text{ erg}$ or $7.5 \times 10^{38} \text{ erg hr}^{-1}$ (assuming a typical emission bandwidth $\Delta\nu \approx 100 \text{ MHz}$). If we naively assume that the luminosity beaming enhancement and radio bursts missed due to beaming cancel out, as well as a radio efficiency factor of $\epsilon_{\text{radio}} = 10^{-5}$, we find the external magnetic energy will be depleted on a timescale:

$$\tau \approx 530 \text{ hr} \left(\frac{B_s}{10^{15} \text{ G}} \right)^2 \left(\frac{\epsilon_{\text{radio}}}{10^{-5}} \right) \quad (4)$$

Caveats to this rough approximation include the non-uniformity of burst rate and the unknown beaming characteristics. Nevertheless, this may imply that if a magnetar powers FRB 20220912A, the radio efficiency may be $\epsilon_{\text{radio}} \gg 10^{-5}$, the external magnetic field may be $B \gg 10^{15}$ G, or the external magnetic field is otherwise continuously replenished (e.g., via core field expulsion).

Methods

Westerbork, Onsala & Toruń

The data reduction and burst search analysis at Westerbork, Onsala and Toruń follows our custom pipeline, which has been previously described⁵. At these three telescopes, we captured and stored the raw voltages (waveform data) in .VDIF format³⁸, with dual circular polarisations and 2-bit sampling. In order to search for bursts, we converted the .VDIF data to 8-bit total intensity (Stokes I) SIGPROC filterbank files using `digi.fil`³⁹. In order to limit dispersive smearing within a channel we made filterbanks with different time and frequency resolutions for searches at different observing bands. For C-band observations, we made filterbanks with 4 μ s time bins and 250 kHz wide frequency channels. For L-band observations at Toruń this was 8 μ s time bins and 62.5 kHz channels and for Westerbork 64 μ s time bins and 62.5 kHz channels; while for P-band we used 512 μ s time bins and 7.8125 kHz channels.

We used `Heimdall` to search for bursts in the filterbank files. In order to minimise the amount of false positive candidates we set a signal-to-noise (S/N) threshold of 7 and limit the dispersion measure (DM) search to within ± 50 pc cm⁻³ of the reported value of $DM_{\text{FRB}} = 220$ pc cm⁻³²³. We mitigate radio frequency interference (RFI) by applying a static mask, which excises certain frequency channels known to contain RFI. The identified burst candidates are then classified using the machine learning classifier `FETCH`⁴⁰, where we make use of models A & H and set a detection threshold of 50%. The burst candidates that have a reported probability of at least 50% in one of the two models are then all manually inspected. As a fail-safe we also manually inspect all burst candidates that have a reported DM within 5 pc cm⁻³ of the expected DM.

Using the radiometer equation we calculate both the detection and completeness thresholds for the observations⁴¹. The detection threshold represents the minimal fluence that our telescopes are sensitive to, while the completeness threshold represents the minimal fluence where we expect to detect (almost) all bursts. For the detec-

tion threshold we assume a 7- σ detection with a canonical adopted FRB width of 1 ms. For the completeness threshold we assume a conservative 15- σ threshold and take a burst width of 3 ms since we know that bursts originating from FRB 20220912A have generically longer durations than one millisecond²⁷. The various detection and completeness thresholds of the instruments, per observing band, are listed in Table 1.

Stockert

At Stockert we record 32-bit total intensity data using the Pulsar Fast Fourier Transform (PFFTS) backend⁴². These data are stored in PFFTS format. Using the `filterbank` tool from the SIGPROC package, we create `filterbank` files that consist of 32-bit floats. The time- and frequency resolution of the filterbanks are 218.45 μ s and 586 kHz, respectively. We then search for bursts using tools from the PRESTO package⁴³. The `rfifind` tool is used to mitigate RFI, `prepsubband` then dedisperses the data using a DM of $DM_{\text{FRB}} = 220$ pc cm⁻³, and finally we search for burst candidates using `single_pulse_search` with a S/N limit of 8. Reported burst candidates are then classified using `FETCH` Model A and a detection threshold of 50%. All automatically classified burst candidates are then manually inspected. The detection and completeness threshold are listed in Table 1.

Observational pointing

Westerbork and Toruń pointed towards RA=23^h09^m05.6^s Dec=+48°42'00.0" (J2000), as published in the discovery report by McKinven & CHIME/FRB Collaboration²³. Onsala pointed towards RA=23^h09^m05.49^s Dec=+48°42'25.6" (J2000), the initial localisation as reported by DSA-110⁴⁴. Stockert initially also pointed towards the CHIME localisation, but changed this to the DSA-110 localisation after 21 December 2022. Even though there was an erratum for the DSA-110 localisation⁴⁵, we did not change our pointing. Regardless, the offset between the pointing directions of the telescopes and the best-known position of FRB 20220912A is less

than $\sim 30''$ in all cases²⁵. This pointing offset is still well within the full-width at half maximum primary beams at different wavelengths, which range from 0.1° (C-band) to 2.3° (P-band).

Digitisation artefacts

We record voltage data at Westerbork, Onsala and Toruń in 2-bit sampling mode. The low bit depth leads to a relatively modest data rate (~ 500 GB/h for $\Delta\nu \sim 128$ MHz), which allows us to observe at a high cadence and process the data with low latency. The downside of the 2-bit sampling, however, is the limited dynamic range of the samples. Digitisation artefacts can manifest in the data in case the power of a burst is concentrated in both time and frequency, for example during strong scintillation^{5,46}. This effect can in turn result in underestimation of the energies of the bursts. We do not observe any digitisation artefacts in the 32-bit data recorded by Stockert.

The behaviour and proposed treatment of digitisation artefacts in 2-bit sampled data has been described by Jenet & Anderson⁴⁷ (see their Section 4.1 and Figure 4). In essence, the 2-bit digitiser has a non-linear response to the received power, which causes the digitised signal to be underestimated compared with the total power of the un-digitised signal. This effect scales with the brightness of the signal and manifests itself as decreased power during the time of the bursts, especially during bright scintillation. This decreased power is visible as ‘depressions’ in the dynamic spectrum and ‘dips’ in the frequency-averaged time series before and after the burst. In our observing setup, we quantise our data per subband, typically 8–32 MHz, with the result that the digitisation artefacts do not span or affect the entire observing bandwidth but are limited per subband, as visible in the top three subbands for burst B68-Wb in Figure 1.

One way to correct for the digitisation artefacts is by using a dynamic level-setting scheme. This method will counter the ‘depression’ area around the signal, but a byproduct of this method is an increase of power around the signal, which is known as quantisation noise. When applying

the dynamic level-setting this increase in power is scattered uniformly across the bandwidth (in our case across a subband). Therefore, the power of the signal will be artificially increased and overestimated. This effect is best visible in the time series of a burst where power is increased before and after the burst; see Extended Data Figure 4 in Ref⁵.

To best estimate the power of a signal we therefore need to remove the scattered quantisation noise. This is done using a scattered power correction (SPC) algorithm, which has been implemented in the DSPSR software package and is applied on a per-subband basis for our recording setup.

We create three different data products, following the same methodology we employed in Ref.⁵. For Method I, we use the Super FX Correlator (SFXC). We coherently (within each frequency channel) and incoherently (between frequency channels) correct the data for dispersion⁴⁸. SFXC does not apply a dynamic level-setting scheme to the data, which means that the ‘dips’ and ‘depressions’ are still present in the data. Subsequently, for Method II we process the bursts using *digifil*, which does apply dynamic level-setting and introduces quantisation noise. Lastly, for Method III we apply the SPC algorithm to the data products made using *digifil* in order to compensate for the quantisation noise.

In Extended Data Figure 2, we show the ratio of fluences relative to those measured using Method III for bursts detected at L-band and P-band. For L-band, we find that applying Method I underestimates the fluences by up to 40%, while Method II overestimates them by up to 10%. For P-band, these digitisation effects are less apparent which is most likely due to the longer dispersive sweep of the burst and low sensitivity of the P-band receiver at Wb.

Fiducial dispersion measure

To correct for the dispersive delay we used a single DM for all bursts detected at L-band (1.4 GHz). The value we used is $219.375 \text{ pc cm}^{-3}$, which was determined by Ref.⁴⁹ from analysis of

the extremely bright and broad-band microshots in a burst that was co-detected by NRT (B2 in that paper) and Westerbork (B52-Wb here). Applying this best-fit DM on bursts detected at P-band (330 MHz) leaves a residual dispersive sweep, as seen in Figure 3. To find the best-fit DM we dedispersed the burst to a range of trial DM values ranging from 219.665 to 219.799 pc cm^{-3} and measured the peak S/N value at each trial DM. We subsequently fitted a Gaussian to the S/N-DM curve and found a best-fit DM value of 219.735 pc cm^{-3} , as shown in Figure 3. While the DM of FRB 20220912A is known to vary⁴⁹, we find that such variations have a negligible effect on the inferred fluences and hence energetics of the bursts, which is the main focus of this paper. Hence, we do not attempt to derive an optimal DM for each burst.

Burst properties

The burst properties we use in our analyses were determined using the filterbank files created with `digifil` and the SPC-algorithm, previously referred to as Method III. RFI was mitigated by manually masking affected frequency channels for all bursts using the tools `psrzap` and `pazi` from the DSPSR software package. Additionally, we also zapped the edges of the subbands because of the drop in sensitivity at these frequencies (see, e.g., B35-st and B15-tr in Figure 1).

To measure the time and frequency extent of the bursts we follow our earlier work⁵. We manually determined the start and stop times of each individual component of a burst. For these time ranges we calculate the 2D auto-correlation function in time and frequency. We then fit a 1D Gaussian to the spectra and time series and determine the width both in time and frequency. We define the burst frequency extent to be the full extent of the observing frequency if the full width at half maximum (FWHM) of the Gaussian fit is more than 75 % of the total bandwidth. The fluence of a burst is determined using the radiometer equation and calculating the flux density per time bin while summing over the on-time region for each component⁴¹. An overview of burst properties can be

found in Supplementary Table 2.

Additionally, we also measured the fluences using filterbank files created by SFXC (Method I) and only `digifil` (Method II) in order to compare and quantify the digitisation effects. The ratios of fluences between the three methods are shown in Figure 2. We find that we encounter saturation effects that underestimate the fluences by up to 40 % (SFXC) and overestimate them by 10 % (`digifil`) for bursts detected at L-band (left panel). For bursts detected at P-band (right panel) the saturation effect is less apparent even though we detect bright bursts ($> 1000 \text{ Jy ms}$). This lack of saturation is most likely due to the longer dispersive sweep of the burst and the relatively low sensitivity of the Westerbork P-band receiver.

Times of arrival

When determining the time of arrival (ToA) of a burst one has to take into account potential data loss during the recording of the `.VDIF` format data. `digifil` currently has no functionality to account for potential data loss that occurred during an observation. Instead, when creating a filterbank file, `digifil` will stitch together gaps in the data. In order to correct for this issue, we determined the ToAs of our detected bursts using SFXC. SFXC has the functionality to accurately handle data loss by padding the missing data with zero values. We create coherent dedispersed filterbank files for bursts observed with Wb and Tr at a time resolution of 64 μs for L-band bursts and 512 μs for P-band bursts. For St, missing data is padded in real time. Both programs use the same assumed dispersive constant of $1/(2.41 \times 10^{-4}) \text{ MHz}^2 \text{ pc}^{-1} \text{ cm}^3 \text{ s}$. We fit a Gaussian to every component in the time series for each burst. We define the ToA of a component as the centre of this fitted Gaussian and we set the ToA of a single burst as the centre of the Gaussian in case of a single component burst or the middle point between the left and right-most component in the case of a multi-component burst. For the case of SFXC, the timestamps are reported with respect to the geocenter of

the Earth with the reference frequency being the middle of the top subband. For `digifil`, the timestamps are local arrival times and the reference frequency is the middle of the top frequency channel. For both cases, we convert the arrival times to barycentric arrival times in the TDB timescale with respect to infinite frequency for the assumed DM for L-band and P-band. An overview of all determined ToAs, per burst and per component, can be found in Table 2.

Cumulative burst rates

The cumulative burst distribution of FRBs is sometimes fit by a single power law $R (> E_\nu) \propto E_\nu^{\gamma_C}$, as has been done, e.g., for FRB 20121102A⁵⁰ and FRB 20200120E⁵¹. Here R is the rate of bursts, E_ν the spectral energy density of the bursts, and γ_C is the slope of the cumulative distribution. To be able to compare distributions between telescopes, we express the energetics of the bursts as spectral energy density (erg/Hz), $E_\nu = E/\nu$. Where ν is the observed bandwidth of the burst. We convert the measured fluences to spectral energy via³⁷,

$$E_\nu = \frac{\mathcal{F} \cdot 4\pi D_L^2}{(1+z)^{2+\alpha}} \quad (5)$$

where \mathcal{F} is the fluence of the burst, $4\pi D_L^2$ is the luminosity distance factor assuming isotropic emission, and $(1+z)^{2+\alpha}$ is the redshift correction, where α is the spectral index ($\mathcal{F}_\nu \propto \nu^\alpha$). We set $\alpha = 0$ to be consistent with respect to the fluence calculation. The fluence is calculated based on the band-averaged time series where we thus assume $\alpha = 0$. The luminosity distance (D_L) of FRB 20220912A is 362.4 Mpc, with corresponding redshift $z = 0.0771$ ⁵².

To fit a power law to the cumulative distribution, we exclude bursts that were detected below our completeness threshold for St, Wb, and Tr; see Table 1 for an overview of completeness thresholds per telescope and observing band. The sensitivity of NRT and FAST enables the detection of bursts of much lower spectral energy density ($E_{\min} \sim 10^{28} - 10^{29}$ erg/Hz) where the cumulative distribution has been shown to deviate from

a single power law¹⁷. In this work, we focus on a turnover towards the higher energies. Therefore, we use the Python package `powerlaw`⁵³ to determine the minimum energy (E_{\min}) above which the distribution is best described by a power law. For FAST we find $E_{\min}^{\text{FAST}} = 5.6 \times 10^{29}$ erg/Hz and for NRT we find $E_{\min}^{\text{nc}} = 3.4 \times 10^{29}$ (erg/Hz). An initial guess of the power law index is estimated using a maximum likelihood method^{54,55}. Next, we use `scipy.optimize.curvefit` to fit a power law, where we assume a fiducial uncertainty of 20% on the energy of the burst. This uncertainty stems mainly from the uncertainty on the system equivalent flux density (SEFD) of each telescope. The error from `curvefit` is the first error we quote. In addition to the 1σ error quoted by `curvefit` we perform a bootstrapping method to estimate the variance of the fit. Bootstrapping is done by refitting the data with only a subset of the data points. We refitted the data 1000 times using 90% of the data points without replacement. The error determined via bootstrapping is noted as the second error quoted on the derived values. We find that the burst energy distribution of NRT is not well described by a single power law. This is apparent by eye, and by calculating the power-law slope using the maximum likelihood method as a function of the spectral energy density, as shown in the right panel of Extended Data Figure 4. We therefore fit a broken power law to the distribution and determine the breakpoint to be $E_{\text{break}} \sim 3.2 \times 10^{30}$ erg/Hz. To be consistent in our methodology, we fit two separate power laws to the NRT data. For the first power law, for bursts that satisfy $E_{\min}^{\text{NRT}} < E_\nu^{\text{NRT}} < E_{\text{break}}$, we find $\gamma_C^{\text{NRT-1}} = -1.69 \pm 0.01 \pm 0.05$. We fit a second power law for bursts that satisfy $E_{\text{break}} < E_\nu^{\text{nc}}$ and find $\gamma_C^{\text{NRT-2}} = -0.60 \pm 0.08 \pm 0.05$, as shown in the left panel of Extended Data Figure 4.

Turnover at the characteristic energy

To investigate a possible turnover in the energy distribution, we combined detections from multiple observational studies constrained in time between MJD 59868 and MJD 59910. These studies were the NRT sample²⁷, detections from ATA²²

and FAST²⁶, as well as the detections described in this work. We filtered out 5 duplicate bursts that were co-detected by the ATA and Stockert and only used the brightest detection in each case. We only consider bursts with energies larger than the completeness threshold of the least sensitive telescope (Westerbork at 24.4 Jy ms), see Table 1. Finally, we converted all fluences to spectral energy densities following Equation 5. We assume a Schechter function⁵⁶ as,

$$P(E_\nu) = N \left(\frac{E_\nu}{E_{\text{char}}} \right)^{\gamma_D} \exp \left[-\frac{E_\nu}{E_{\text{char}}} \right] \quad (6)$$

where E_ν is the spectral energy density (erg/Hz), γ_D is the slope on the differential distribution, E_{char} is the cut-off energy, and N is a normalisation factor. We apply a Markov Chain Monte Carlo (MCMC) fitting technique to test if the combined burst sample is well described by a Schechter function. We used the `emcee` package⁵⁷, and initialise the MCMC chains by finding starting parameters using `lmfit`. The fit parameters are sampled from uniform priors. We set the limits on E_{char} to be larger than 0 and smaller than 10^{35} erg/Hz. We ran 100 walkers for 10000 steps and discard the first 500 steps attributed to the burn-in phase. We plot the MCMC results using the `corner` package⁵⁸, as shown in the left panel of Figure 3.

Maximum redshift

Following a method employed in earlier work⁵, we can place a limit on the maximum observable redshift based on our brightest detections at both 1.4 GHz and 330 MHz. Our brightest detection at 1.4 GHz is burst B68-Wb with a reported fluence of 1587 Jy ms (or $E_\nu = 2.2_{-0.4}^{+0.4} \times 10^{32}$ erg/Hz). FAST is the most sensitive telescope currently operating at this wavelength range, with a completeness threshold of 54 mJy ms³¹. B68-Wb would therefore still be detected by FAST if FRB 20220912A would have been at a redshift of $z = 9.9_{-1.1}^{+1.1}$ and the burst was emitted at ~ 14 GHz.

At 330 MHz our brightest detection is burst B128-Wb with a measured fluence of 2629 Jy ms (or $E_\nu = 3.6_{-0.7}^{+0.7} \times 10^{32}$ erg/Hz). With the reported

detection limit of CHIME/FRB of 1 Jy ms²³, burst B128-Wb would still have been observable if the source was placed at redshift $z = 2.8_{-0.3}^{+0.3}$ with an implied emitting frequency of ~ 1.2 GHz. Although the majority of CHIME sources do not have measured redshifts, their highest measured DM source, FRB 20180906B, is consistent with originating in the aforementioned redshift range with an estimated redshift of $z = 2.95$ ⁵⁹. CHIME is not detecting a large population of these high-redshift sources¹⁶. This could be related to the large scattering for high-redshift FRBs ($z > 1$) at the observing frequency of CHIME⁶⁰.

Detection and sky rate

We observed FRB 20220912A for 1158.57 and 607.34 unique hours at L- and P-band, respectively, and detected 13 and 7 bursts above a fluence $\mathcal{F} > 500$ Jy ms. This implies a detection rate of $0.27_{-0.13}^{+0.19}$ burst/day (L-band) and $0.28_{-0.17}^{+0.29}$ burst/day (P-band) for high-fluence bursts, where the errors are the 95% Poisson uncertainty on the rates. Though the burst rates are consistent between the two bands, we caution that these multi-frequency observations were not strictly simultaneous and both reflect an average rate over some range of time (Figure 1).

Based on the ASKAP Fly Eye's survey³² and modelled number counts⁶¹ assuming a burst energy distribution with slope $\gamma_C = -1.5$, an all-sky rate at L-band has been determined above a fluence $\mathcal{F} > 100$ Jy ms, $R_{\text{sky}}(\mathcal{F} > 100 \text{ Jy ms}) = 5 \times 10^3 \text{ sky}^{-1} \text{ yr}^{-1}$. We detected 48 L-band bursts above 100 Jy ms, which corresponds to a rate of $7.3_{-1.9}^{+2.4} \% R_{\text{sky}}(\mathcal{F} > 100 \text{ Jy ms})$ and agrees with the all-sky rate for the ATA sample of $5.8_{-2.4}^{+3.4} \%$ ²² (quoted errors are the 95% Poisson uncertainty on the rates). For our brightest detections, 13 bursts above 500 Jy ms and 4 bursts above 1000 Jy ms, we find an all-sky rate of $22.0_{-10.3}^{+15.6} \% R_{\text{sky}}(\mathcal{F} > 500 \text{ Jy ms})$ and $19.1_{-13.9}^{+29.8} \% R_{\text{sky}}(\mathcal{F} > 1000 \text{ Jy ms})$, respectively. A similar calculation has been done for the all-sky rate contribution for FRB 20201124A with a fluence larger than 500 Jy ms and was estimated to be $2.6_{-2.0}^{+5.0} \% R_{\text{sky}}(\mathcal{F} > 500 \text{ Jy ms})$ ⁵.

This illustrates that the contribution to the all-sky rate of FRB 20220912A was almost an order of magnitude higher compared to FRB 20201124A for highly energetic bursts. Additionally, it underlines that a single hyperactive FRB repeater can strongly contribute to the all-sky rate for a relatively short time when the source is active. The upcoming, wide-field BURSTT²⁹ telescope (FoV $\sim 10^4$ deg²) should be an excellent system for identifying such sources.

Multi-wavelength counterparts

Multi-wavelength counterparts to FRBs are expected within both magnetospheric^{19,62} and particularly maser shock models¹². Simultaneous X-ray counterparts, as observed for the FRB-like burst from SGR 1935+2154^{63–65} and prompt optical afterglows from FRB-associated flares^{66–68} are the most likely detectable counterparts to extragalactic FRBs.

Constraints on high-energy counterparts have been placed⁶⁹ for bursts from the closest repeating extragalactic FRB source: FRB 20200120E at just 3.6 Mpc⁷⁰. The most energetic FRB from this source ($E_{r,B4} = 2.8 \times 10^{33}$ erg) was detected simultaneous to NICER observations, broadly ruling out any simultaneous giant or intermediate magnetar X-ray flares⁶⁹. The most energetic bursts presented in this work are roughly 7 orders of magnitude larger in total radio energy, at a distance approximately 100 times greater meaning, for similar radio efficiencies, multi-wavelength fluxes coincident with the brightest bursts presented here should be a factor $\sim 10^3$ times higher. This bolsters the case for sensitive X-ray observations of prolific repeaters known to produce very bright bursts, notwithstanding the challenging large required time on source.

In Extended Data Figure 5 we show the predicted approximate optical (680 nm) afterglow lightcurves of B68-Wb and B128-Wb following previous maser shock afterglow formulations^{68,71}. In lieu of an X-ray detection, we normalize the lightcurves assuming an unobserved, quasi-simultaneous X-ray counterpart a factor L_X/L_r more luminous than the FRB. We also show 5σ

upper limits obtained by the ATLAS telescope network⁷² the night following B68-Wb in the ‘orange’ 560 – 820 nm band, and include representative limiting magnitudes of the ARCTIC telescope⁷³, which has previously been utilized to constrain optical FRB afterglows⁶⁷.

Energy distributions of pulsars

Some pulsars that emit giant pulses (GPs) also show a burst distribution that could be described with a break and flattening toward higher energies. For PSR B1937+21 a break occurs in the cumulative distribution for pulses with a pulse energy larger than $7 \text{ Jy } \mu\text{s}$ ⁷⁴. These results were not found in previous studies on this pulsar^{75,76}, which could be due to the much shorter exposure times. The cumulative distribution of PSR B0540–69 does show a flattening in the distribution for higher energetic bursts⁷⁷. Another well-studied emitter of GPs is PSR B0531+21 (the Crab Pulsar). The term ‘supergiant pulse’ was coined for pulses that show inconsistency with the probability implied by a simple power law⁷⁸. These findings of a flattening were confirmed after 100 hours of observing with the Green Bank telescope⁷⁹. A more recent study did not find any hint of flattening in the distribution of supergiant pulses ($\mathcal{F} > 130 \text{ Jy ms}$) after observing the Crab pulsar for 260 hours¹⁰. Although we see similarities between FRBs and pulsars in their cumulative energy distributions, their energies differ by at least four orders of magnitude. A shared rotationally powered emission mechanism between pulsars and FRBs is ruled out; it is more likely that FRBs are magnetically powered⁸⁰. To our knowledge, systematic flattening of pulsar energy distributions at high energies has not been studied in detail for a population of sources.

Data availability

The data that support the plots within this paper and other findings of this study are available under <https://doi.org/10.5281/zenodo.11261763> [Published prior to publication] or from the corresponding author upon reasonable request.

Code availability

The scripts and jupyter notebooks used to analyse the data, generate the plots and tables with the burst properties are available at [github-link will be provided prior to publication]. The pipeline written to process and search the baseband data can be found at <https://github.com/pharaofranz/frb-baseband.jive5ab> can be found on <https://github.com/jive-vlbi/jive5ab>, Heimdall is hosted at <https://sourceforge.net/projects/heimdall-astro/> and FETCH can be found at <https://github.com/devanshkv/fetch>. The pulsar package DSPSR is hosted at <https://sourceforge.net/projects/dpspr/> and SIGPROC can be retrieved from <https://github.com/SixByNine/sigproc>. The source code for the MCMC analysis is based on <https://philuttley.github.io/stats-methods-24/12-mcmc/index.html>

Acknowledgements

We thank the directors and staff of the participating telescopes for allowing us to observe with their facilities. We thank Willem van Straten for modifying the DSPSR software package to fit our needs and for helping us with the SPC-algorithm. We thank Kaitlyn Shin and Zorawar Wadiasingh for insightful discussions. We thank Daniela Huppenkothen and Phil Uttley for discussions regarding MCMC analysis and fitting of the energy distribution. This work is supported by the NWO XS grant: WesterFlash (OCENW.XS22.1.053; PI: Kirsten). The AstroFlash research group at McGill University,

University of Amsterdam, ASTRON, and JIVE is supported by: a Canada Excellence Research Chair in Transient Astrophysics (CERC-2022-00009); the European Research Council (ERC) under the European Union’s Horizon 2020 research and innovation programme (‘EuroFlash’; Grant agreement No. 101098079); and an NWO-Vici grant (‘AstroFlash’; VI.C.192.045). A. J. C. acknowledges support from the Oxford Hintze Centre for Astrophysical Surveys which is funded through generous support from the Hintze Family Charitable Foundation. This work is based in part on observations carried out using the 32-m radio telescope operated by the Institute of Astronomy of the Nicolaus Copernicus University in Toruń (Poland) and supported by a Polish Ministry of Science and Higher Education SpUB grant. We express our gratitude to the operators and observers of the Astropeller Stockert telescope: Thomas Buchsteiner, Bert Engelskirchen, Elke Fischer, Hans-Peter Löge, Thomas Nitsche and Kevin Schmitz. F. K. acknowledges support from Onsala Space Observatory for the provisioning of its facilities/observational support. The Onsala Space Observatory national research infrastructure is funded through Swedish Research Council grant No 2017-00648. This work makes use of data from the Westerbork Synthesis Radio Telescope owned by ASTRON. ASTRON, the Netherlands Institute for Radio Astronomy, is an institute of the Dutch Scientific Research Council NWO (Nederlandse Organisatie voor Wetenschappelijk Onderzoek). We thank the Westerbork operators Richard Blaauw, Jurjen Sluman and Henk Mulders for scheduling and supporting observations. K. N. is an MIT Kavli Fellow. Z. P. is supported by an NWO Veni fellowship (VI.Veni.222.295).

Author contributions

O. S. O. B coordinated the observational campaign, and led the observations at Westerbork. He also led the data analysis, created the majority of the figures and tables, and wrote most of the manuscript. P. C. provided essential guidance on the data analysis and interpretation and con-

tributed to the writing. J. W. T. H. supervised and guided the work, interpreted the data scientifically and made significant contributions to the writing. A. J. C. made significant contributions to the writing and created Figure 4 and Extended Data Figure 5. M. P. G. led and W. P. supported the observations and burst searching at Toruń. W. H. led the observations and burst searching at Stockert. F. K. led the observations and burst searching at Onsala. All co-authors provided input on the scientific interpretation and commented on the paper.

Competing interests

The authors declare no competing interests.

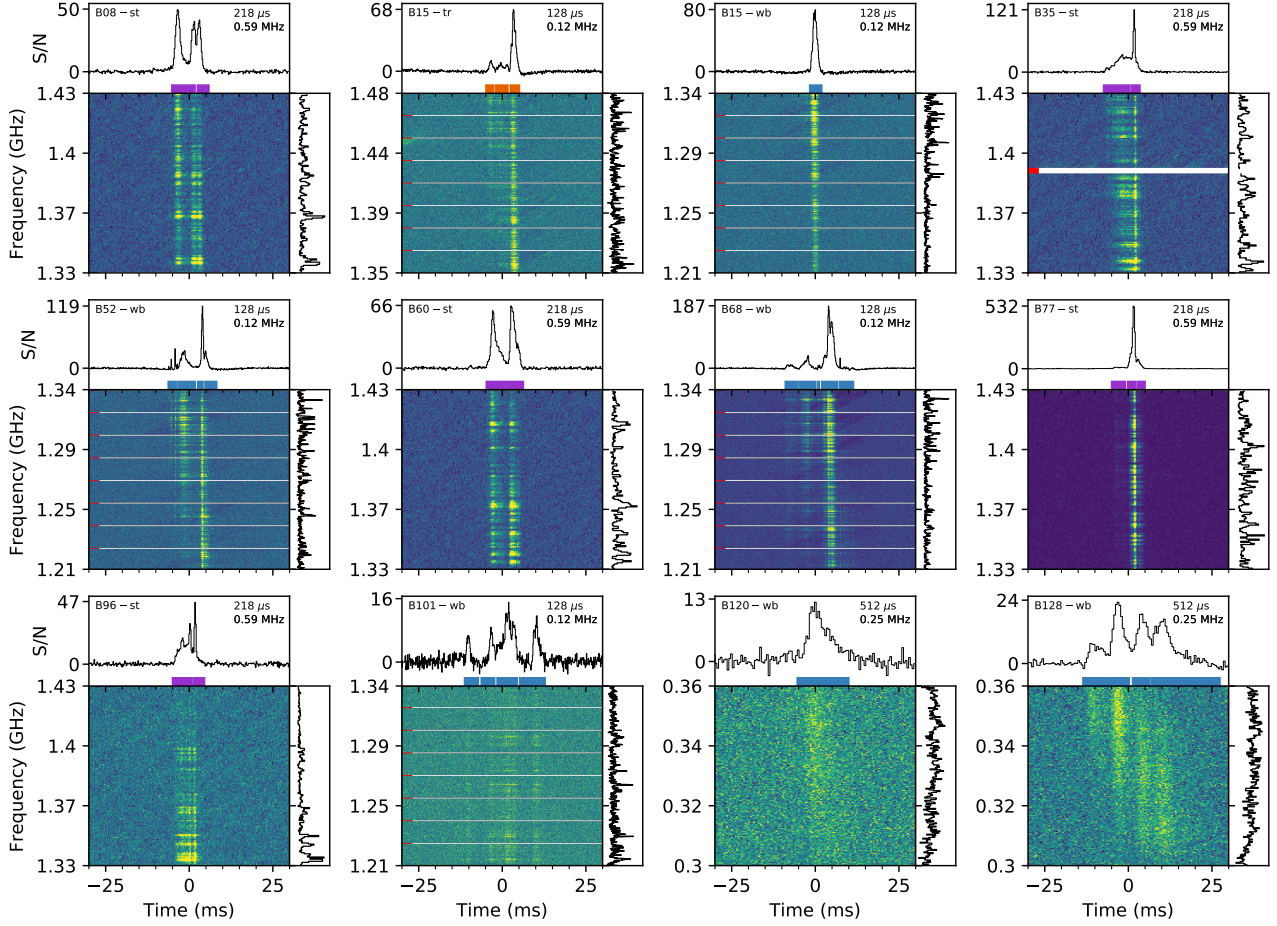


Figure 1: Dynamic spectra, time and temporal profiles for a subset of bursts

Each sub figure consists of three panels. Shown in the top panel is the burst-id, the time- and frequency resolution at which the data is plotted and the time profile of the burst. The colored bars represent the width for each component of a burst whereas the color of the bars correspond the instrument used to detect the burst. Purple corresponds to Stockert (St), orange to Toruń (Tr) and blue to Westerbork (Wb). The side panel shows the temporal profile which is the sum over the time axis, but only under the colored bars. The white vertical lines are masked channels at the edges of the subbands or the presence of radio frequency interference (RFI) which are indicated by red ticks. The bursts have been corrected for dispersive effects where we used a value of $219.37 \text{ pc cm}^{-3}$ for bursts detected at 1.4 GHz (L-band) and $219.73 \text{ pc cm}^{-3}$ for bursts detected at 0.3 GHz (P-band). For Stockert this correction was applied incoherently (between frequency channels) and for Toruń and Westerbork this correction was applied incoherently and coherently (within frequency channels)

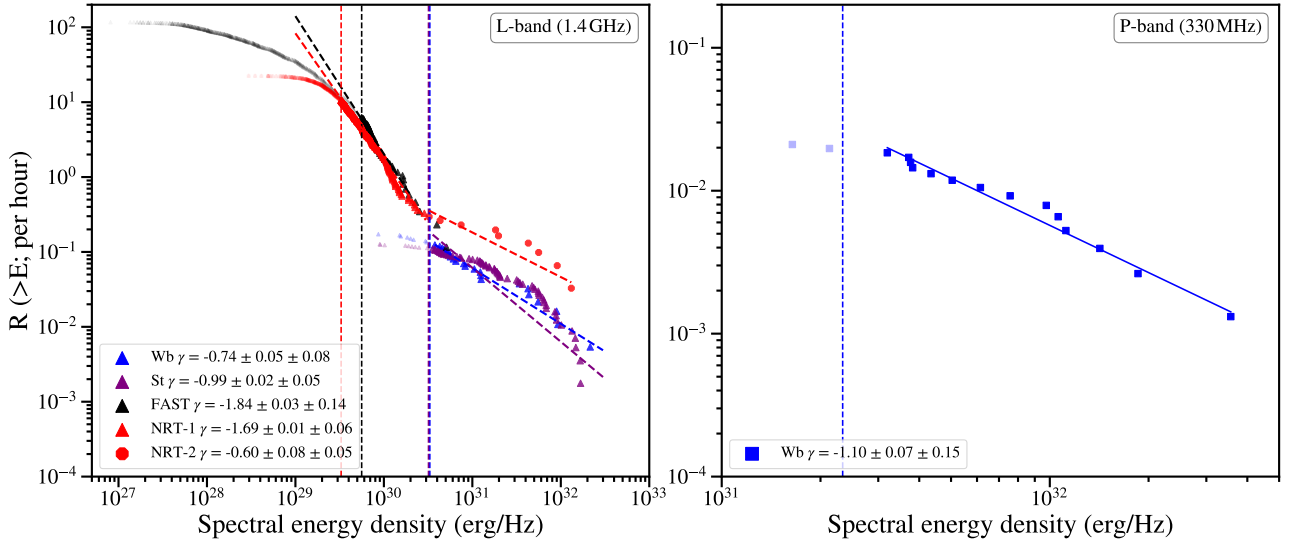


Figure 2: **Cumulative burst energy distribution of spectral energy densities.**

In the left panel we show detections by Westerbork (Wb) and Stockert (St), FAST²⁶ and NRT²⁷ at 1.4 GHz (L-band). In order compare between the different observational campaigns we only show bursts that were observed between MJD 59869 and 59910. Comparing the different rates reveals a break in the distribution towards higher energies ($\sim 3 \times 10^{30}$ erg/Hz). The purple and blue vertical line correspond to the completeness threshold as indicated in Table 1. The red and black vertical lines denote the point where the distribution can be best described by a single power law as calculated by the Python package `powerlaw`. Transparent data points which are on the left side of the vertical lines were excluded in the fit. When fitting we set a 20% error on the energies and quote two errors. The first error is the 1σ statistical uncertainty on the fit and the second error is the 1σ error after the bootstrapping method. In the right panel we show detections observed at 0.3 GHz (P-band).

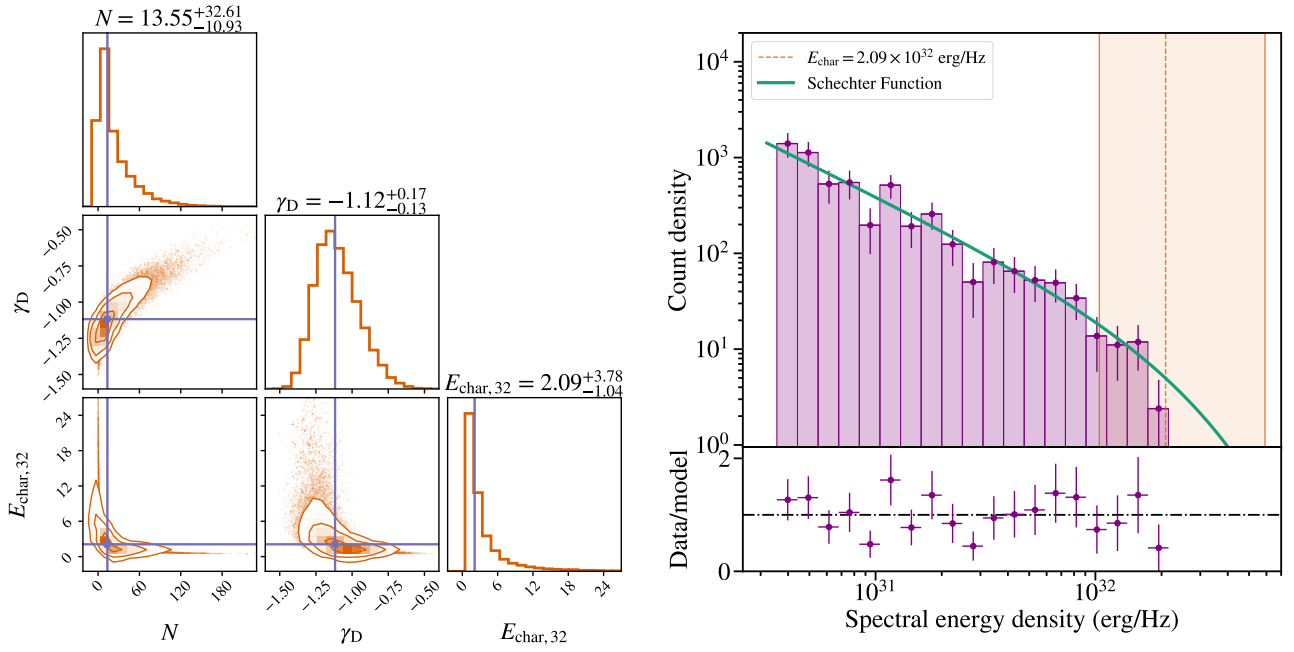


Figure 3: **Spectral energy densities modelled by a Schechter function.**

Left: corner plot of the results from the MCMC analysis, thinned by a factor 30 for visual purposes. The solid lines denote the median values of the posterior distributions and the errors are the 16 % and 84 % quantile. Right: The differential distribution in the top panel includes bursts above 3.3×10^{30} erg/Hz (or 24.4 Jy ms) detected by Westerbork, Stockert, Toruń, NRT, ATA and FAST between MJD 59869 and 59910. The green line is an over-plotted Schechter function based on the median values of the posterior distribution of the MCMC analysis. The vertical orange dashed line is the best fit value for the characteristic energy with the coloured region corresponding to error region of the 16 % and 84 % quantile. The bottom panel shows the ratio between the data and the Schechter model.

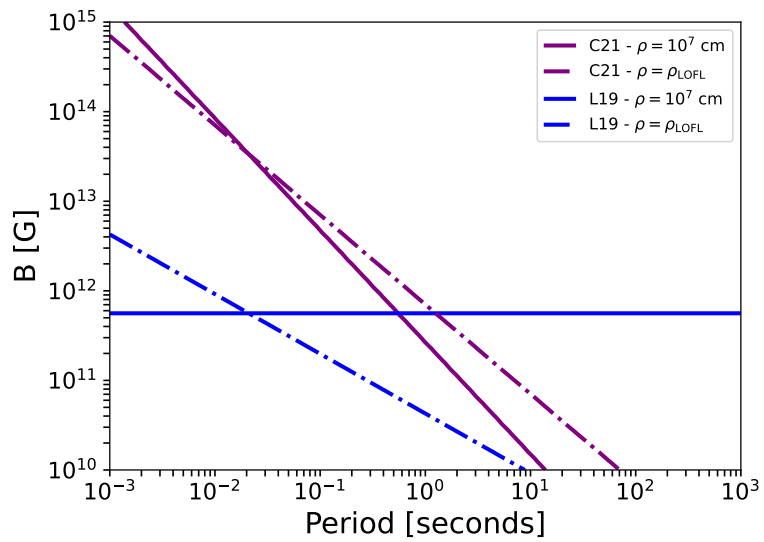


Figure 4: **Magnetic field constraints for B77-St**

Minimum local magnetic field B as a function of neutron period for B77-St assuming coherent curvature radiation^{19,36}. Solid lines refer to fixed field line curvature radius of $\rho_c = 10^7$ cm, dot-dashed lines refer to emission along the last open field line at the polar cap co-latitude.

Table 1: **Observational set-up**

Station ^a	Band	Frequency [MHz]	Bandwidth ^b [MHz]	Bandwidth per subband [MHz]	SEFD ^c [Jy]	Detection ^d threshold [Jy ms]	Completeness ^e threshold [Jy ms]	Completeness ^f threshold [10^{30} erg Hz ⁻¹]	Time observed ^g [hr]
Wb	P	300–356	50	8	2100	46.5	172.5	23.36	607.34
Wb	L _{wb}	1259–1387	100	16	420	6.6	24.4	3.30	196.58
St	L _{st}	1332.5–1430.5	90	98	385	6.4	23.6	3.20	933.53
Tr	L _{Tr-1}	1290–1546	200	32	350	3.9	14.4	1.95	3.23
Tr	L _{Tr-2}	1350–1478	100	16	350	5.5	20.3	2.75	268.10
Tr	C _{Tr-1}	4550–4806	200	32	220	2.4	7.9	1.07	40.39
Tr	C _{Tr-2}	4600–4728	100	32	220	3.4	11.3	1.53	113.87
O8	C _{O8}	4798.5–5054.5	200	32	480	5.3	17.4	2.36	28.36
Total time at 1.4 GHz (L-band) on source [hr] ^h									1159
Total telescope time/total time on source [hr] ^h									2192/1491

^a Wb: Westerbork RT1, St: Stockert, Tr: Toruń, O8: Onsala 25 – m

^b Effective bandwidth accounting for RFI and band edges.

^c From the [EVN status page](#) (with the exception of St).

^d Assuming a 7σ detection threshold and a typical FRB pulse width of 1 ms.

^e Assuming a 15σ detection threshold and a width of 3 ms.

^f Fluence completeness converted using equation 5.

^g Hours spend on source between MJD 59867 and 59983 (15 October 2022 and 08 February 2023).

^h Total time on source accounts for overlap between the participating telescopes.

Table 2: **Best Schechter fit results from different studies**

	$\log_{10} E^{\text{char}}$ [erg] ^a	γ_D^b	\mathcal{F}_{min} [Jy ms] ^e
This work	$41.32^{+0.45}_{-0.30}$	$-1.12^{+0.17}_{-0.13}$	24.4
Ryder et al. (2023) ^{21,c}	$41.7^{+0.2}_{-0.2}$
Shin et al. (2023) ¹⁶	$41.38^{+0.51}_{-0.50}$	$-1.30^{+0.7}_{-0.4}$	5.0
James et al. (2022) ¹⁵	$41.26^{+0.72}_{-0.22}$	$-1.95^{+0.18}_{-0.15}$	0.5/4.4/21.9 ⁸¹
Luo et al. (2020) ^{20,d}	$42.08^{+0.30}_{-0.06}$	$-1.79^{+0.31}_{-0.35}$	0.55

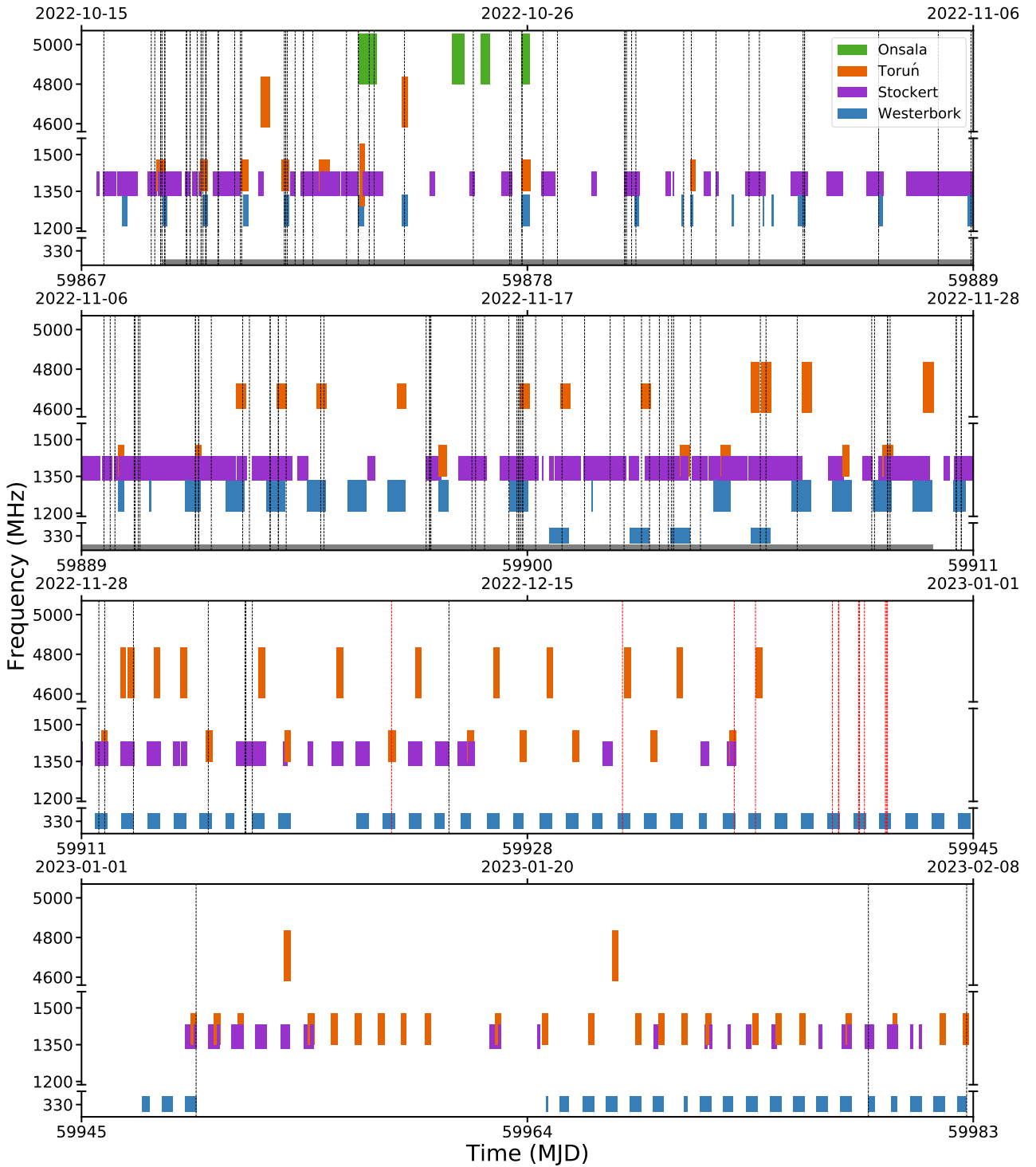
^aEnergy assuming a conical adopted bandwidth of 1 GHz.

^bBest fitted slope parameters on a differential distribution.

^cBased on the sample of James et al. (2022)¹⁵.

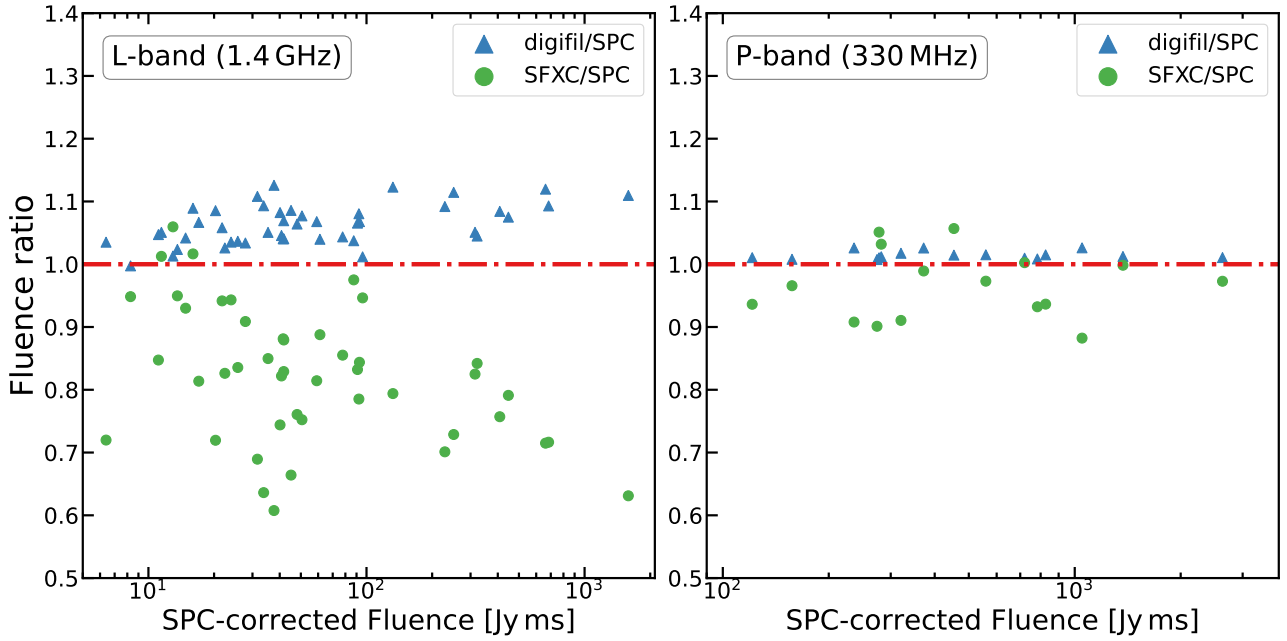
^dLuminosity (L_*) converted using the average width from Table 2 of $\bar{w} = 4.14$ ms.

^eFluence limits on the different observational campaigns.



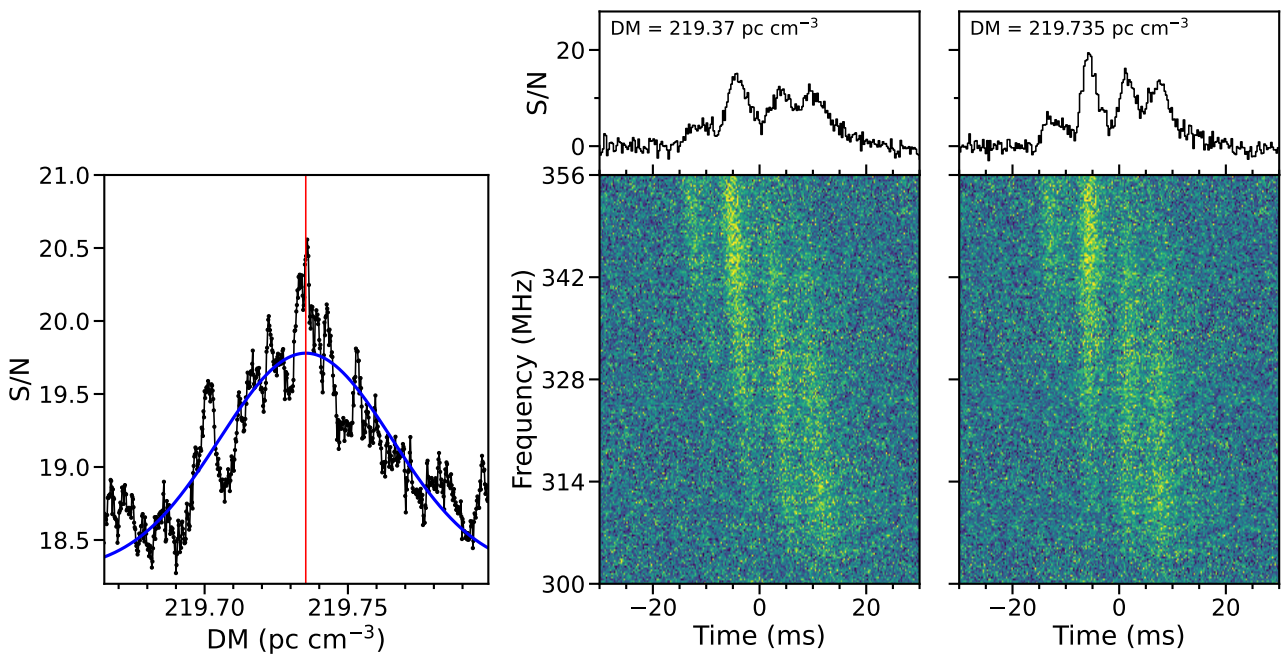
Extended Data Figure 1: **Overview of the FRB 20220912A observing campaign**

Each coloured block represents an observation with a telescope at a certain frequency. The top two panels show 22 days and the bottom two panels show 36 days with the associated MJD and and calendar dates on the x-axis. The broken y-axis show the frequency range. The vertical dotted lines denote detections of bursts where black illustrates detections at L-band (1.4 GHz) and red detections at P-band (0.3 GHz). The black bar in the top panels indicate the overlapping observing window with FAST and NRT.



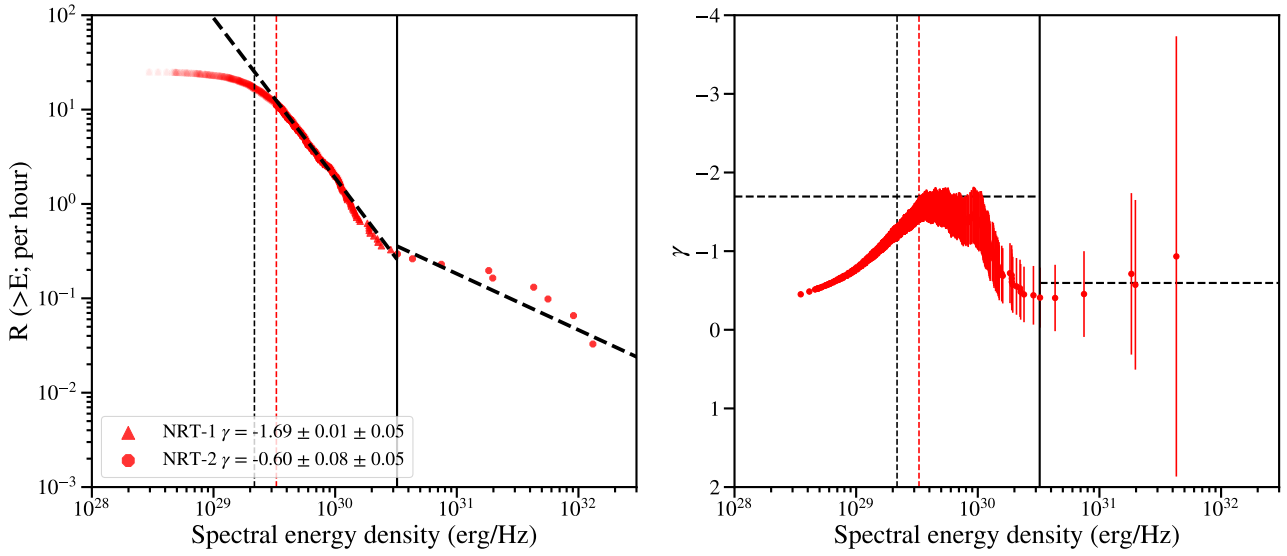
Extended Data Figure 2: **Ratio of fluences computed from SFXC- and digifil-generated filterbanks.**

The fluence for each burst was measured three different ways due to digitisation artefacts present in the data. These filterbanks were made for bursts detected with Westerbork and Toruń using SFXC, digifil and digifil with a scattered power correction (SPC) applied. Here we plot the ratio of these measured fluences for L-band (left panel) and P-band (right panel). For L-band we find that due to digitisation effects the fluence of the burst can be underestimated for up to 40% (SFXC) and overestimated for 10% (digifil). Applying the SPC algorithm to correct for digitisation effects is therefore essential. Even though we detect bright (> 1000 Jy ms) bursts at P-band, these digitisation effects are less apparent, this most likely due to longer dispersive sweep of the burst and the low sensitivity of the Westerbork P-band receiver.



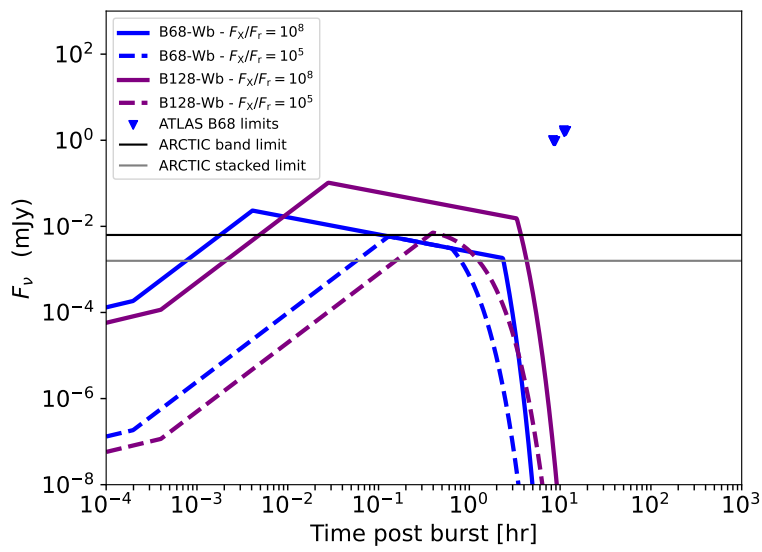
Extended Data Figure 3: **DM determination for bursts detected at P-band.**

Peak signal-to-noise (SN) versus dispersion measure (DM) curve for our brightest detection at P-band, burst B128-Wb. When applying the DM used to correct for dispersive delay for bursts detected at L-band, $219.37 \text{ pc cm}^{-3}$, there still was a residual sweep present for bursts detected at P-band, as illustrated in the middle panel. By correcting the burst for range of DM values and fitting a Gaussian to the SN-curve we find a best fit DM of $219.735 \text{ pc cm}^{-3}$ and shown in the right panel.



Extended Data Figure 4: **Cumulative burst energy distribution for bursts detected by NRT.**

Left: The cumulative energy distribution for NRT, also shown in Figure 2, fitted with two power laws. The vertical dotted black line is the estimated completeness threshold and the vertical dotted red line indicates the turnover point as estimated using the `powerlaw` package. The solid black line corresponds to the determined breakpoint of the distribution at $E_{\text{break}} = 3.2 \times 10^{30}$ erg/Hz. Right: the power law index (γ_C) as a function of the spectral energy density calculated by a maximum-likelihood estimation. The horizontal dotted black lines indicate the slopes of the power law used in the left panel.



Extended Data Figure 5: **Predicted optical afterglows for maser shock model**

The predicted optical afterglow from B68-Wb and B128-Wb in the synchrotron maser model framework⁶⁸. We also show 5σ limits obtained by the ATLAS telescope network from 8 hours after B68-Wb, and include typical limiting magnitudes from the ARCTIC telescope which could have been achieved if observations were scheduled rapidly after B68-Wb and B128-Wb⁶⁷.

Supplementary Table 1: Schechter function parameter results

Results and best fit parameters from the MCMC analysis on fitting a Schechter function to the differential burst distribution by varying the fluence/energy threshold for bursts detected between MJD 59869 and 59910. The coloured green row denotes the the completeness threshold and parameter values which were used in Figure 3.

σ Threshold	fluence Threshold [Jy ms]	spectral energy Threshold [10^{30} erg Hz $^{-1}$]	Total Bursts	N_{Wb}	N_{St}	N_{Tr}	N_{ATA}	N_{Nc}	N_{Fast}	N	γ_D	E^{char} [10^{32} erg Hz $^{-1}$]	χ^2_{ν}
10	16.10	2.18	146	25	68	4	13	32	4	$9.68^{+24.87}_{-8.30}$	$-1.14^{+0.14}_{-0.10}$	$2.54^{+6.87}_{-1.33}$	1.13
14.55 ^a	23.81	3.22	130	23	64	2	9	30	2	$12.44^{+25.52}_{-10.14}$	$-1.13^{+0.16}_{-0.12}$	$2.16^{+1.33}_{-1.06}$	0.85
15 ^b	24.40	3.30	125	22	62	2	8	29	2	$13.55^{+32.61}_{-10.93}$	$-1.12^{+0.17}_{-0.13}$	$2.09^{+3.78}_{-1.04}$	0.78
20	32.45	4.40	112	20	55	2	7	27	1	$20.32^{+40.40}_{-16.08}$	$-1.05^{+0.20}_{-0.15}$	$1.68^{+2.70}_{-0.76}$	0.66
30	48.80	6.61	93	12	47	1	7	26	0	$40.06^{+66.02}_{-31.28}$	$-0.90^{+0.28}_{-0.23}$	$1.19^{+1.68}_{-0.49}$	0.50

^aEnergy threshold corresponding the the break-point of the power law determined for NRT, see Figure 4.

^bThe completion threshold corresponding to the least sensitive telescope (Wb). The result of this fit are shown in Figure 3.

Supplementary Table 2: Burst properties

The complete table and an additional table with properties per component for each burst can be found in the supplementary material.

Burst ID [†]	Station	TOA ^a [MJD]	Peak S/N ^b	Fluence ^c [Jy ms]	Number of components	Width ^d [ms]	Spectral density ^e [10^{29} erg Hz $^{-1}$]	Spectral luminosity ^f [10^{32} erg s $^{-1}$ Hz $^{-1}$]	BW ^g [MHz]	Central Frequency [MHz]
B01	St	59867.55026197426	14.90	42.16± 8.43	2	9.61	57.11± 11.42	5.94± 1.19	128	1381
B02	St	59868.72071901775	8.91	24.26± 4.85	1	7.86	32.86± 6.57	4.18± 0.84	128	1381
B03	St	59868.80699833712	4.69	29.73± 5.95	1	13.54	40.27± 8.05	2.97± 0.59	128	1381
B04	St	59868.95206450199	4.41	11.80± 2.36	1	4.59	15.98± 3.20	3.48± 0.70	128	1381
B05	Tr	59868.95206954337	16.67	40.75± 8.15	1	3.97	55.19± 11.04	13.91± 2.78	128	1414
B06	Tr	59868.98521494057	5.89	20.31± 4.06	1	6.14	27.51± 5.50	4.48± 0.90	128	1414
⋮	⋮	⋮	⋮	⋮	⋮	⋮	⋮	⋮	⋮	⋮
B127	Wb	59941.68738958076	6.99	274.25± 54.85	1	20.48	371.47± 74.29	18.14± 3.63	54	328
B128	Wb	59941.73017555207	24.17	2629.40± 525.88	4	32.77	3561.49± 712.30	108.71± 21.74	54	328
B129	St	59949.88269849737	6.78	46.15± 9.23	1	12.67	62.51± 12.50	4.93± 0.99	128	1381
B131	St	59978.53235768391	39.33	375.07± 75.01	1	13.33	508.03± 101.61	38.13± 7.63	128	1381
B132	Tr	59982.71918144583	22.65	50.59± 10.12	1	6.91	68.53± 13.71	9.92± 1.98	128	1414

[†]B84 was omitted due to it later being classified as radio frequency interference (RFI), B130 was removed because the presence of strong RFI made it impossible to measure its properties.

^aTime of arrival referenced to the solar system barycenter at infinite frequency in TDB. We used a dispersion constant of $1/(2.41 \times 10^{-4})$ MHz 2 pc $^{-1}$ cm 3 s.

For detections with a central frequency of 328 MHz we used a DM of 219.735 pc cm $^{-3}$ and the others a DM of 219.37 pc cm $^{-3}$.

^bThe peak S/N of the brightest component.

^cThe sum of the computed fluences for each component measured after applying the SPC algorithm (method III).

We assume a 20% error for all bursts dominated by the uncertainty of the SEFD.

^dThe manually determined time span between the start of the first and end of the last component.

^eComputed using Equation 5, $D_L = 362.4$ Mpc and $z = 0.0771$.

^fSpectral density divided by the width.

^gThe bandwidth of the burst used for the computation of the fluence.

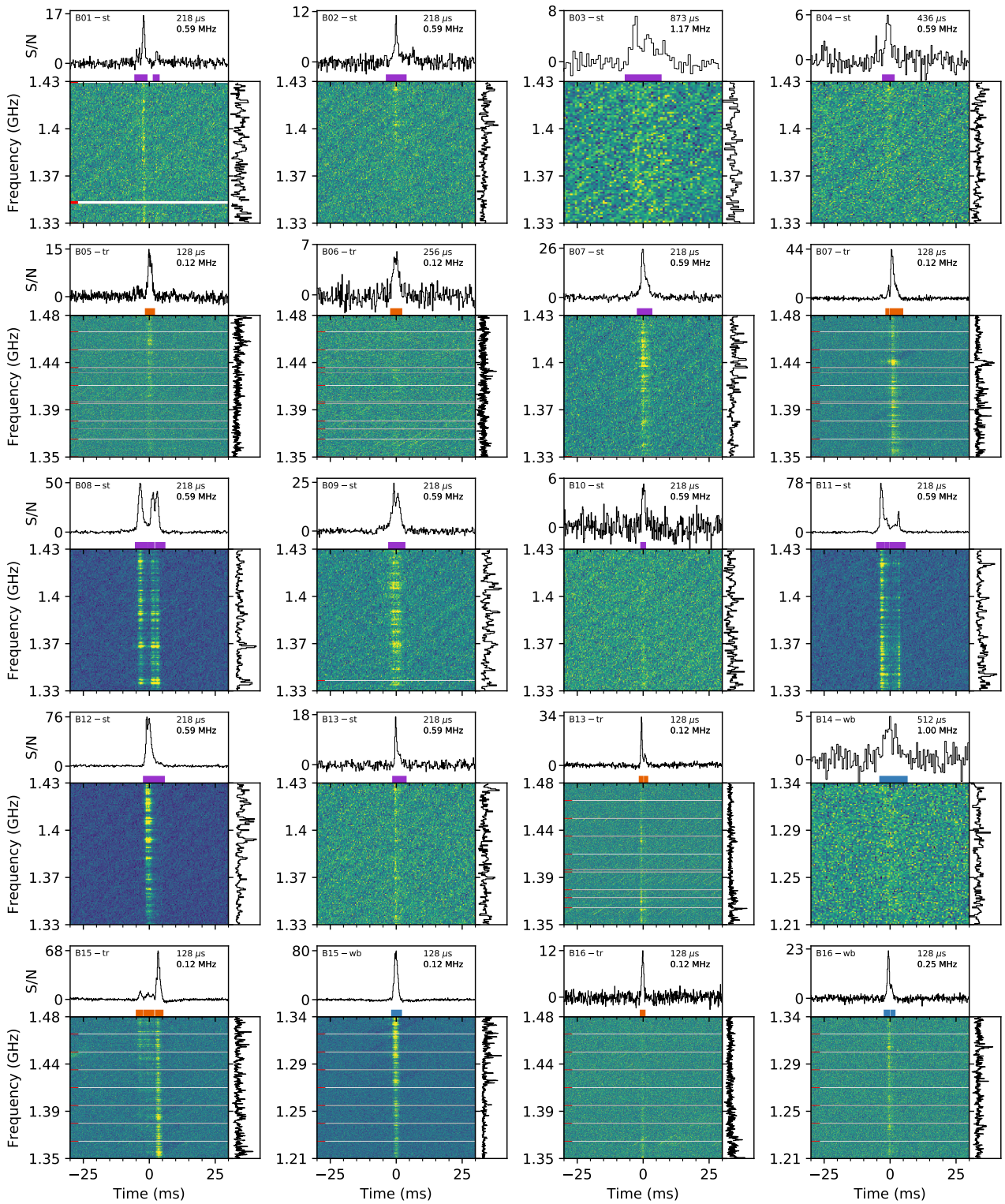
References

- [1] Petroff, E., Hessels, J. W. T. & Lorimer, D. R. Fast radio bursts at the dawn of the 2020s. *Astron. & Astrophys. Rev.* **30**, 2 (2022).
- [2] Snelders, M. P. *et al.* Detection of ultra-fast radio bursts from FRB 20121102A. *Nature Astronomy* **7**, 1486–1496 (2023).
- [3] Chime/Frb Collaboration, B. C., Andersen *et al.* Sub-second periodicity in a fast radio burst. *Nature* **607**, 256–259 (2022).
- [4] Spitler, L. G. *et al.* A repeating fast radio burst. *Nature* **531**, 202–205 (2016).
- [5] Kirsten, F. *et al.* A link between repeating and non-repeating fast radio bursts through their energy distributions. *Nature Astronomy* **8**, 337–346 (2024).
- [6] CHIME/FRB Collaboration *et al.* CHIME/FRB Discovery of 25 Repeating Fast Radio Burst Sources. *Astrophys. J.* **947**, 83 (2023).
- [7] CHIME/FRB Collaboration *et al.* A bright millisecond-duration radio burst from a Galactic magnetar. *Nature* **587**, 54–58 (2020).
- [8] Bochenek, C. D. *et al.* A fast radio burst associated with a Galactic magnetar. *Nature* **587**, 59–62 (2020).
- [9] Gordon, A. C. *et al.* The Demographics, Stellar Populations, and Star Formation Histories of Fast Radio Burst Host Galaxies: Implications for the Progenitors. *Astrophys. J.* **954**, 80 (2023).
- [10] Bera, A. & Chengalur, J. N. Super-giant pulses from the Crab pulsar: energy distribution and occurrence rate. *Mon. Not. R. Astron. Soc.* **490**, L12–L16 (2019).
- [11] Kirsten, F. *et al.* Detection of two bright radio bursts from magnetar SGR 1935 + 2154. *Nature Astronomy* **5**, 414–422 (2021).
- [12] Metzger, B. D., Margalit, B. & Sironi, L. Fast radio bursts as synchrotron maser emission from decelerating relativistic blast waves. *Mon. Not. R. Astron. Soc.* **485**, 4091–4106 (2019).
- [13] Mereghetti, S. *et al.* INTEGRAL Discovery of a Burst with Associated Radio Emission from the Magnetar SGR 1935+2154. *Astrophys. J. Lett.* **898**, L29 (2020).
- [14] Kaspi, V. M. & Beloborodov, A. M. Magnetars. *Annu. Rev. Astron. Astrophys.* **55**, 261–301 (2017).
- [15] James, C. W. *et al.* A measurement of Hubble’s Constant using Fast Radio Bursts. *Mon. Not. R. Astron. Soc.* **516**, 4862–4881 (2022).
- [16] Shin, K. *et al.* Inferring the Energy and Distance Distributions of Fast Radio Bursts Using the First CHIME/FRB Catalog. *Astrophys. J.* **944**, 105 (2023).
- [17] Li, D. *et al.* A bimodal burst energy distribution of a repeating fast radio burst source. *Nature* **598**, 267–271 (2021).
- [18] Lu, W., Kumar, P. & Narayan, R. Fast radio burst source properties from polarization measurements. *Mon. Not. R. Astron. Soc.* **483**, 359–369 (2019).
- [19] Cooper, A. J. & Wijers, R. A. M. J. Coherent curvature radiation: maximum luminosity and high-energy emission. *Mon. Not. R. Astron. Soc.* **508**, L32–L36 (2021).
- [20] Luo, R. *et al.* On the FRB luminosity function - - II. Event rate density. *Mon. Not. R. Astron. Soc.* **494**, 665–679 (2020).
- [21] Ryder, S. D. *et al.* A luminous fast radio burst that probes the Universe at redshift 1. *Science* **382**, 294–299 (2023).
- [22] Sheikh, S. Z. *et al.* Characterization of the repeating FRB 20220912A with the Allen Telescope Array. *Mon. Not. R. Astron. Soc.* **527**, 10425–10439 (2024).

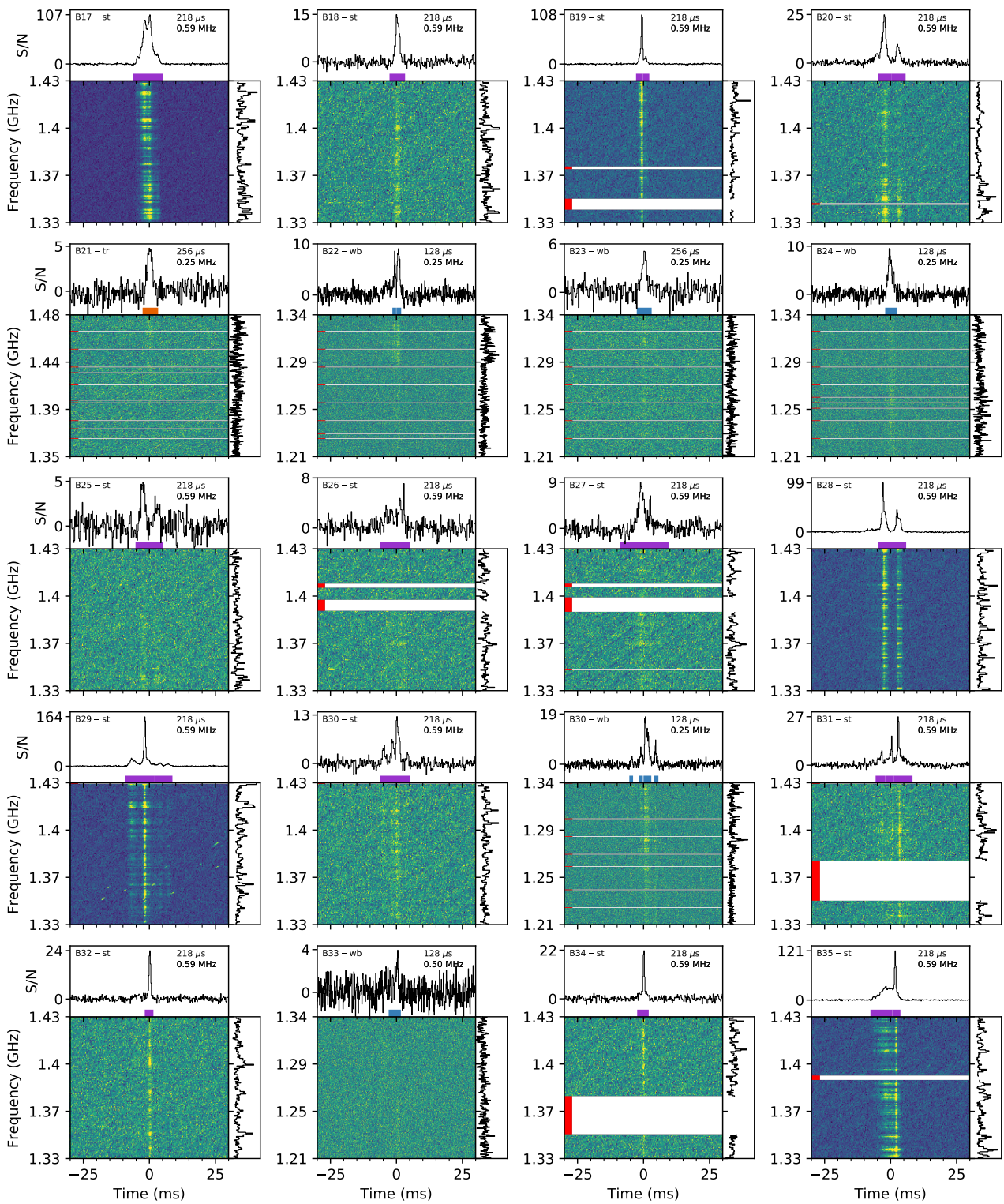
- [23] McKinven, R. & CHIME/FRB Collaboration. Nine Bursts in Three Days from a Newly Discovered Repeating Source of Fast Radio Bursts. *The Astronomer's Telegram* **15679**, 1 (2022).
- [24] Ravi, V. *et al.* Deep Synoptic Array Science: Discovery of the Host Galaxy of FRB 20220912A. *Astrophys. J. Lett.* **949**, L3 (2023).
- [25] Hewitt, D. M. *et al.* Millisecond localization of the hyperactive repeating FRB 20220912A. *Mon. Not. R. Astron. Soc.* **529**, 1814–1826 (2024).
- [26] Zhang, Y.-K. *et al.* FAST Observations of FRB 20220912A: Burst Properties and Polarization Characteristics. *Astrophys. J.* **955**, 142 (2023).
- [27] Konijn, D. C. *et al.* A Nançay Radio Telescope study of the hyperactive repeating FRB 20220912A. Preprint at [arXiv:2407.10155](https://arxiv.org/abs/2407.10155) (2024).
- [28] Vanderlinde, K. *et al.* The Canadian Hydrogen Observatory and Radio-transient Detector (CHORD). In *Canadian Long Range Plan for Astronomy and Astrophysics White Papers* volume 2020 28 (2019).
- [29] Lin, H.-H. *et al.* BURSTT: Bustling Universe Radio Survey Telescope in Taiwan. *Publ. Astron. Soc. Pac.* **134**, 094106 (2022).
- [30] Lin, H.-H. *et al.* Do All Fast Radio Bursts Repeat? Constraints from CHIME/FRB Far Side-Lobe FRBs. Preprint at [arXiv:2307.05261](https://arxiv.org/abs/2307.05261) (2023).
- [31] Xu, H. *et al.* A fast radio burst source at a complex magnetized site in a barred galaxy. *Nature* **609**, 685–688 (2022).
- [32] Shannon, R. M. *et al.* The dispersion-brightness relation for fast radio bursts from a wide-field survey. *Nature* **562**, 386–390 (2018).
- [33] Wadiasingh, Z. *et al.* The Fast Radio Burst Luminosity Function and Death Line in the Low-twist Magnetar Model. *Astrophys. J.* **891**, 82 (2020).
- [34] Kumar, P., Lu, W. & Bhattacharya, M. Fast radio burst source properties and curvature radiation model. *Mon. Not. R. Astron. Soc.* **468**, 2726–2739 (2017).
- [35] Wang, W.-Y., Xu, R. & Chen, X. On the Magnetospheric Origin of Repeating Fast Radio Bursts. *Astrophys. J.* **899**, 109 (2020).
- [36] Lu, W. & Kumar, P. The maximum luminosity of fast radio bursts. *Mon. Not. R. Astron. Soc.* **483**, L93–L97 (2019).
- [37] Macquart, J. P. & Ekers, R. FRB event rate counts - II. Fluence, redshift, and dispersion measure distributions. *Mon. Not. R. Astron. Soc.* **480**, 4211–4230 (2018).
- [38] Whitney, A., Kettenis, M., Phillips, C. & Sekido, M. VLBI Data Interchange Format (VDIF). In Navarro, R. *et al.*, editors, *Sixth International VLBI Service for Geodesy and Astronomy. Proceedings from the 2010 General Meeting* 192–196 (2010).
- [39] van Straten, W. & Bailes, M. DSPSR: Digital Signal Processing Software for Pulsar Astronomy. *Pubs. Astron. Soc. Australia* **28**, 1–14 (2011).
- [40] Agarwal, D., Aggarwal, K., Burke-Spolaor, S., Lorimer, D. R. & Garver-Daniels, N. FETCH: A deep-learning based classifier for fast transient classification. *Mon. Not. R. Astron. Soc.* **497**, 1661–1674 (2020).
- [41] Cordes, J. M. & McLaughlin, M. A. Searches for Fast Radio Transients. *Astrophys. J.* **596**, 1142–1154 (2003).
- [42] Barr, E. D. *et al.* The Northern High Time Resolution Universe pulsar survey I. Setup and initial discoveries. *Monthly Notices of the Royal Astronomical Society* **435**, 2234–2245 (2013).
- [43] Ransom, S. PRESTO: PulsAR Exploration and Search TOOLkit. Astrophysics Source Code Library, record ascl:1107.017 (2011).

- [44] Ravi, V. Detection and localization of FRB 20220912A with DSA-110. *The Astronomer's Telegram* **15693**, 1 (2022).
- [45] Ravi, V. Erratum to ATel #15693. *The Astronomer's Telegram* **15716**, 1 (2022).
- [46] Ikebe, S. *et al.* Detection of a bright burst from the repeating fast radio burst 20201124A at 2 GHz. *PASJ* **75**, 199–207 (2023).
- [47] Jenet, F. A. & Anderson, S. B. The Effects of Digitization on Nonstationary Stochastic Signals with Applications to Pulsar Signal Baseband Recording. *Publ. Astron. Soc. Pac.* **110**, 1467–1478 (1998).
- [48] Keimpema, A. *et al.* The SFXC software correlator for very long baseline interferometry: algorithms and implementation. *Experimental Astronomy* **39**, 259–279 (2015).
- [49] Hewitt, D. M. *et al.* Dense forests of microshots in bursts from FRB 20220912A. *Mon. Not. R. Astron. Soc.* **526**, 2039–2057 (2023).
- [50] Gourdjji, K. *et al.* A Sample of Low-energy Bursts from FRB 121102. *Astrophys. J. Lett.* **877**, L19 (2019).
- [51] Nimmo, K. *et al.* A burst storm from the repeating FRB 20200120E in an M81 globular cluster. *Mon. Not. R. Astron. Soc.* **520**, 2281–2305 (2023).
- [52] Ravi, V. *et al.* The host galaxy and persistent radio counterpart of FRB 20201124A. *Mon. Not. R. Astron. Soc.* **513**, 982–990 (2022).
- [53] Alstott, J., Bullmore, E. & Plenz, D. powerlaw: A Python Package for Analysis of Heavy-Tailed Distributions. *PLoS ONE* **9**, e85777 (2014).
- [54] Crawford, D. F., Jauncey, D. L. & Murdoch, H. S. Maximum-Likelihood Estimation of the Slope from Number-Flux Counts of Radio Sources. *Astrophys. J.* **162**, 405 (1970).
- [55] James, C. W., Ekers, R. D., Macquart, J. P., Bannister, K. W. & Shannon, R. M. The slope of the source-count distribution for fast radio bursts. *Mon. Not. R. Astron. Soc.* **483**, 1342–1353 (2019).
- [56] Schechter, P. An analytic expression for the luminosity function for galaxies. *Astrophys. J.* **203**, 297–306 (1976).
- [57] Foreman-Mackey, D., Hogg, D. W., Lang, D. & Goodman, J. emcee: The mcmc hammer. *PASP* **125**, 306–312 (2013).
- [58] Foreman-Mackey, D. corner.py: Scatterplot matrices in Python. *The Journal of Open Source Software* **1**, 24 (2016).
- [59] Chawla, P. *et al.* Modeling Fast Radio Burst Dispersion and Scattering Properties in the First CHIME/FRB Catalog. *Astrophys. J.* **927**, 35 (2022).
- [60] Ocker, S. K. *et al.* The Large Dispersion and Scattering of FRB 20190520B Are Dominated by the Host Galaxy. *Astrophys. J.* **931**, 87 (2022).
- [61] Lu, W. & Piro, A. L. Implications from ASKAP Fast Radio Burst Statistics. *Astrophys. J.* **883**, 40 (2019).
- [62] Yang, Y.-P. & Zhang, B. Fast Radio Bursts and Their High-energy Counterparts from Magnetar Magnetospheres. *Astrophys. J.* **919**, 89 (2021).
- [63] Ridnaia, A. *et al.* A peculiar hard X-ray counterpart of a Galactic fast radio burst. *Nature Astronomy* **5**, 372–377 (2021).
- [64] Tavani, M. *et al.* An X-ray burst from a magnetar enlightening the mechanism of fast radio bursts. *Nature Astronomy* **5**, 401–407 (2021).
- [65] Li, C. K. *et al.* HXMT identification of a non-thermal X-ray burst from SGR J1935+2154 and with FRB 200428. *Nature Astronomy* **5**, 378–384 (2021).

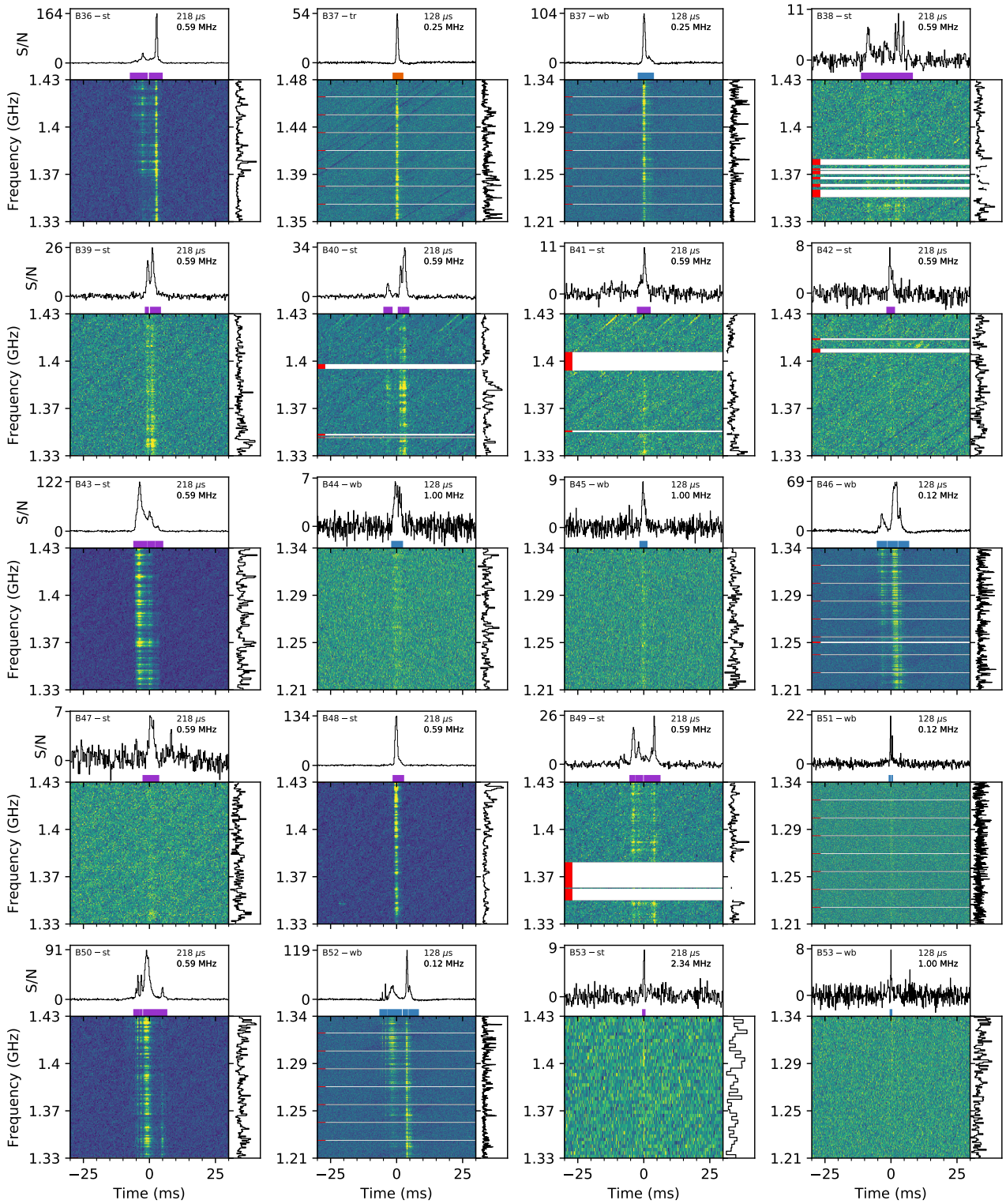
- [66] Lyutikov, M. & Lorimer, D. R. How Else Can We Detect Fast Radio Bursts? *Astrophys. J. Lett.* **824**, L18 (2016).
- [67] Kilpatrick, C. D. *et al.* Deep Optical Observations Contemporaneous with Emission from the Periodic FRB 180916.J0158+65. *Astrophys. J. Lett.* **907**, L3 (2021).
- [68] Cooper, A. J. *et al.* Testing afterglow models of FRB 200428 with early post-burst observations of SGR 1935 + 2154. *Mon. Not. R. Astron. Soc.* **517**, 5483–5495 (2022).
- [69] Pearlman, A. B. *et al.* Multiwavelength Constraints on the Origin of a Nearby Repeating Fast Radio Burst Source in a Globular Cluster. Preprint at [arXiv:2308.10930](https://arxiv.org/abs/2308.10930) (2023).
- [70] Bhardwaj, M. *et al.* A Nearby Repeating Fast Radio Burst in the Direction of M81. *Astrophys. J. Lett.* **910**, L18 (2021).
- [71] Margalit, B., Beniamini, P., Sridhar, N. & Metzger, B. D. Implications of a Fast Radio Burst from a Galactic Magnetar. *Astrophys. J. Lett.* **899**, L27 (2020).
- [72] Tonry, J. L. *et al.* ATLAS: A High-cadence All-sky Survey System. *Publ. Astron. Soc. Pac.* **130**, 064505 (2018).
- [73] Huehnerhoff, J. *et al.* Astrophysical Research Consortium Telescope Imaging Camera (ARCTIC) facility optical imager for the Apache Point Observatory 3.5m telescope. In Evans, C. J., Simard, L. & Takami, H., editors, *Ground-based and Airborne Instrumentation for Astronomy VI* volume 9908 of *Society of Photo-Optical Instrumentation Engineers (SPIE) Conference Series* 99085H (2016).
- [74] McKee, J. W. *et al.* A detailed study of giant pulses from PSR B1937+21 using the Large European Array for Pulsars. *Mon. Not. R. Astron. Soc.* **483**, 4784–4802 (2019).
- [75] Cognard, I., Shrauner, J. A., Taylor, J. H. & Thorsett, S. E. Giant Radio Pulses from a Millisecond Pulsar. *Astrophys. J. Lett.* **457**, L81 (1996).
- [76] Soglasnov, V. A. *et al.* Giant Pulses from PSR B1937+21 with Widths ≤ 15 Nanoseconds and $T_b \geq 5 \times 10^{39}$ K, the Highest Brightness Temperature Observed in the Universe. *Astrophys. J.* **616**, 439–451 (2004).
- [77] Geyer, M. *et al.* The Thousand-Pulsar-Array programme on MeerKAT - III. Giant pulse characteristics of PSR J0540-6919. *Mon. Not. R. Astron. Soc.* **505**, 4468–4482 (2021).
- [78] Cordes, J. M., Bhat, N. D. R., Hankins, T. H., McLaughlin, M. A. & Kern, J. The Brightest Pulses in the Universe: Multifrequency Observations of the Crab Pulsar’s Giant Pulses. *Astrophys. J.* **612**, 375–388 (2004).
- [79] Mickaliger, M. B. *et al.* A Giant Sample of Giant Pulses from the Crab Pulsar. *Astrophys. J.* **760**, 64 (2012).
- [80] Lyutikov, M. Fast Radio Bursts’ Emission Mechanism: Implication from Localization. *Astrophys. J. Lett.* **838**, L13 (2017).
- [81] James, C. W. *et al.* The z-DM distribution of fast radio bursts. *Mon. Not. R. Astron. Soc.* **509**, 4775–4802 (2022).



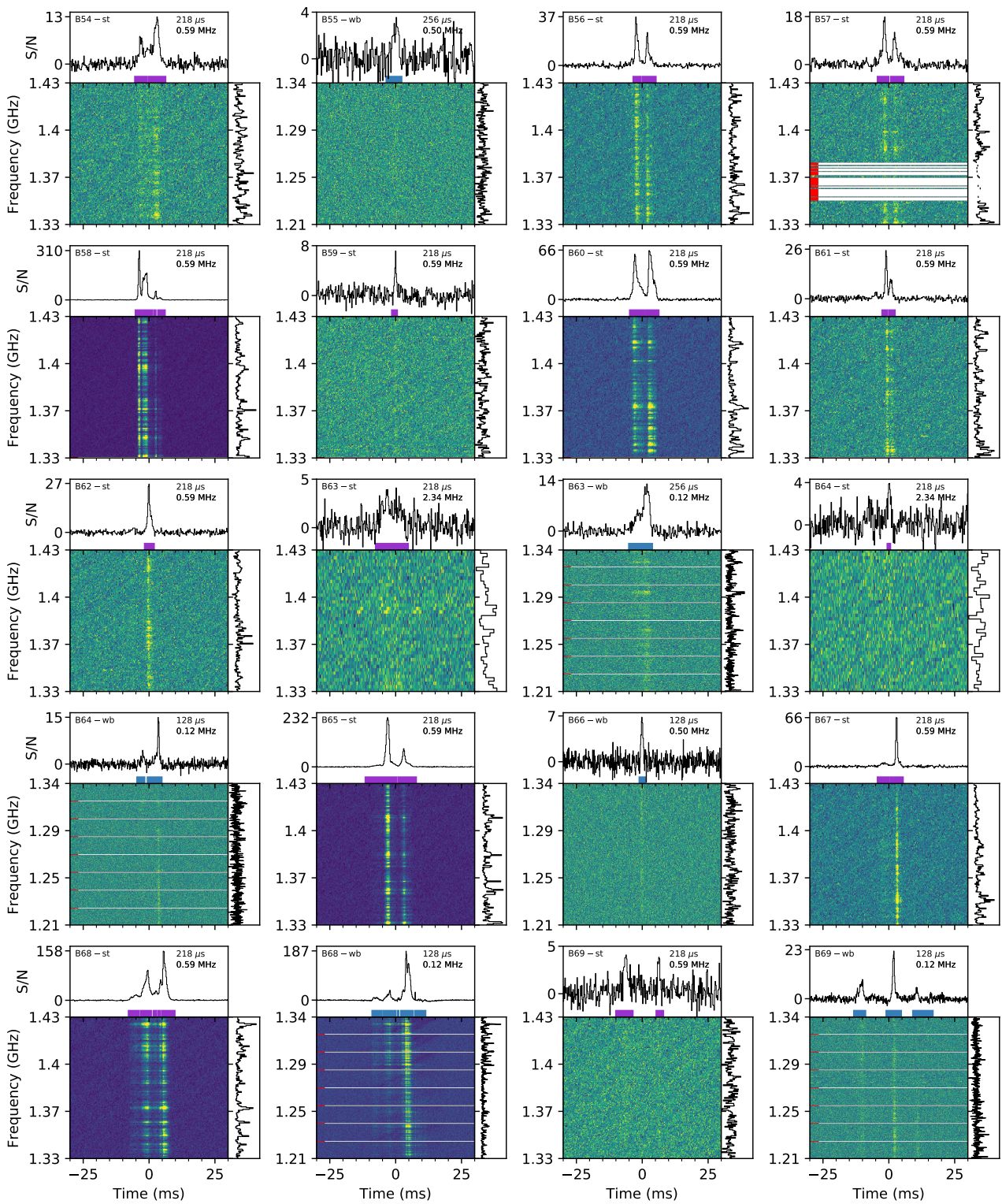
Supplementary Data Figure 1: Dynamic spectra, time and temporal profiles for all bursts, see Figure 1 for a full description of the panels.



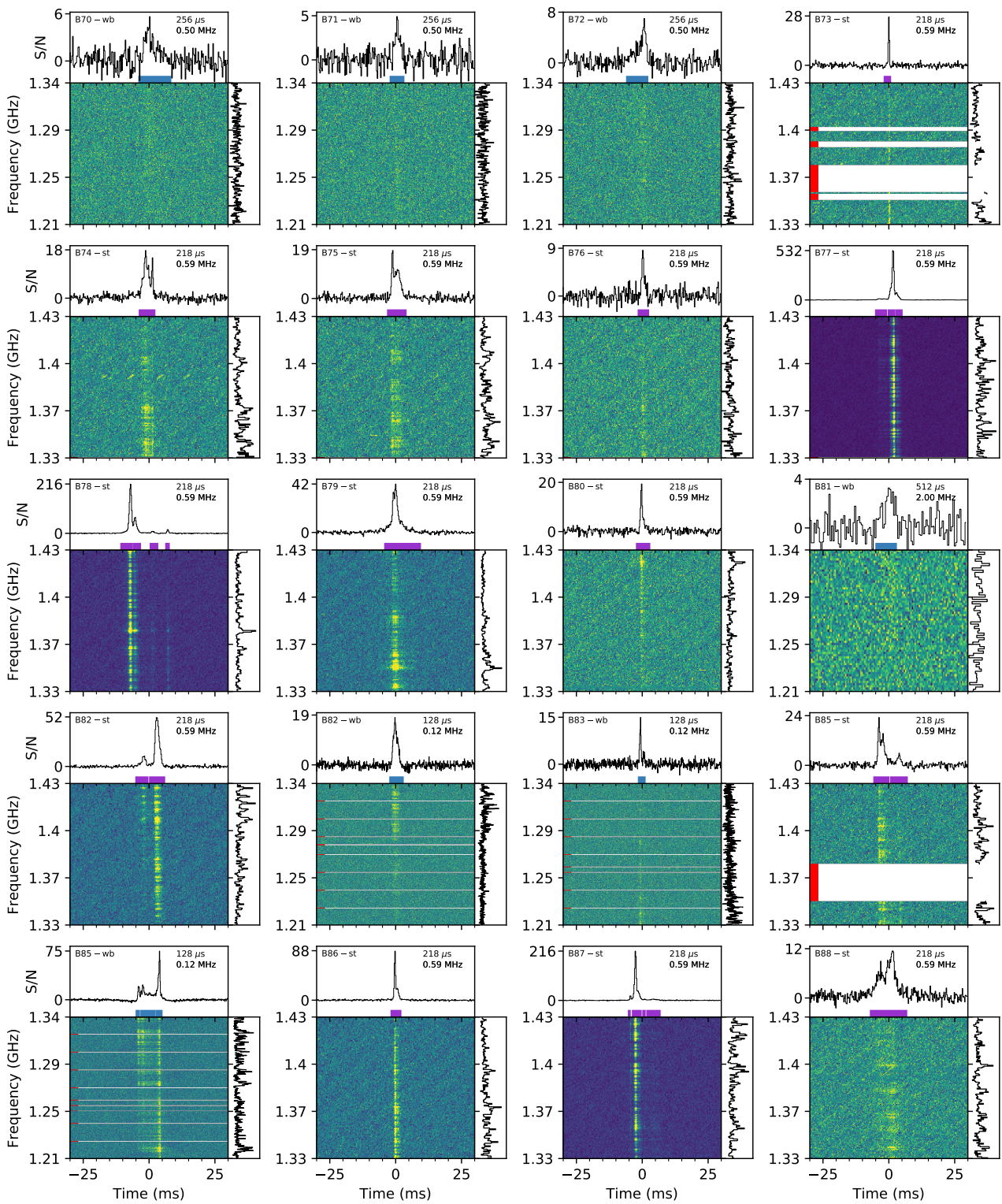
Supplementary Data Figure 1 (Cont.)



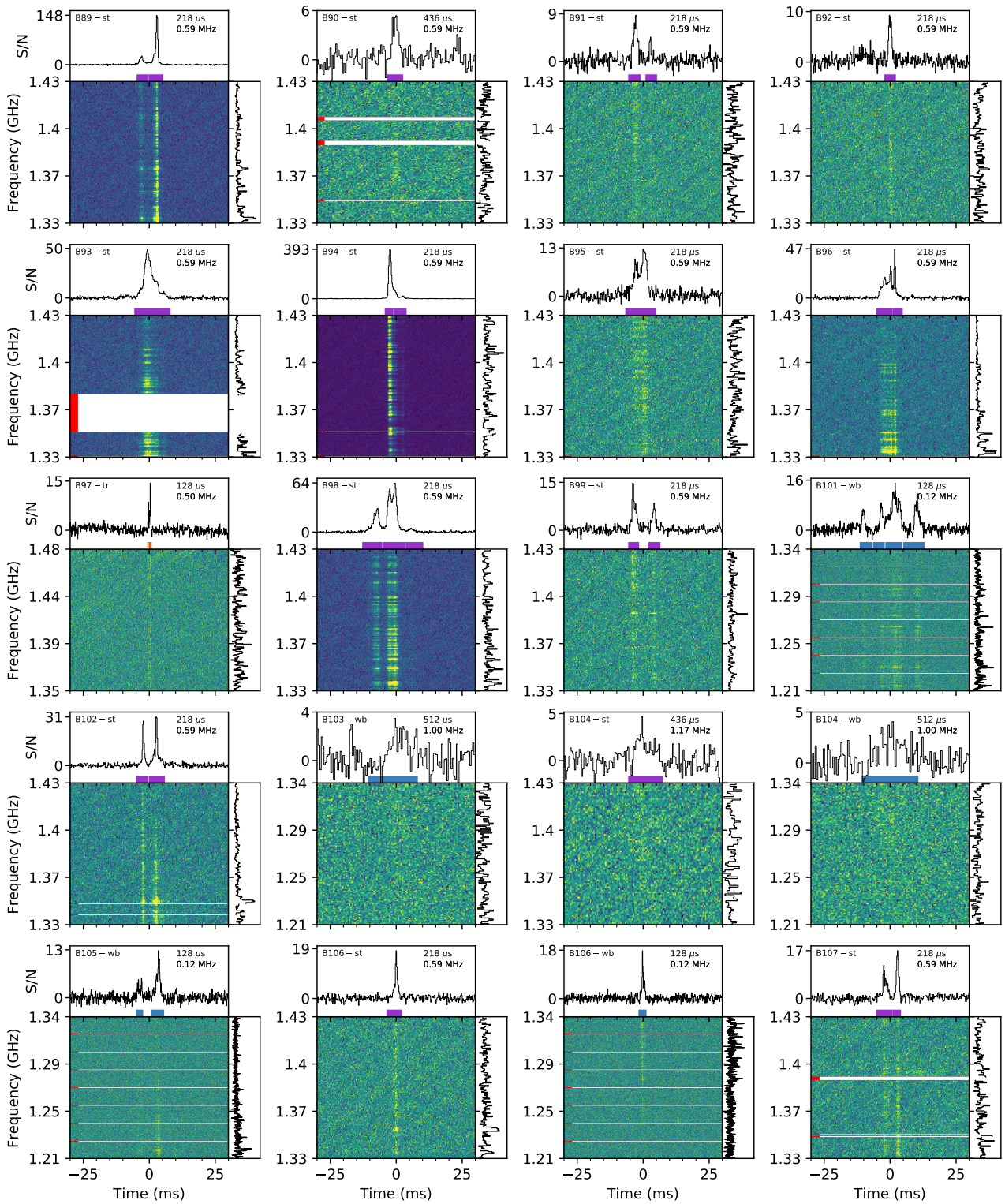
Supplementary Data Figure 1 (Cont.)



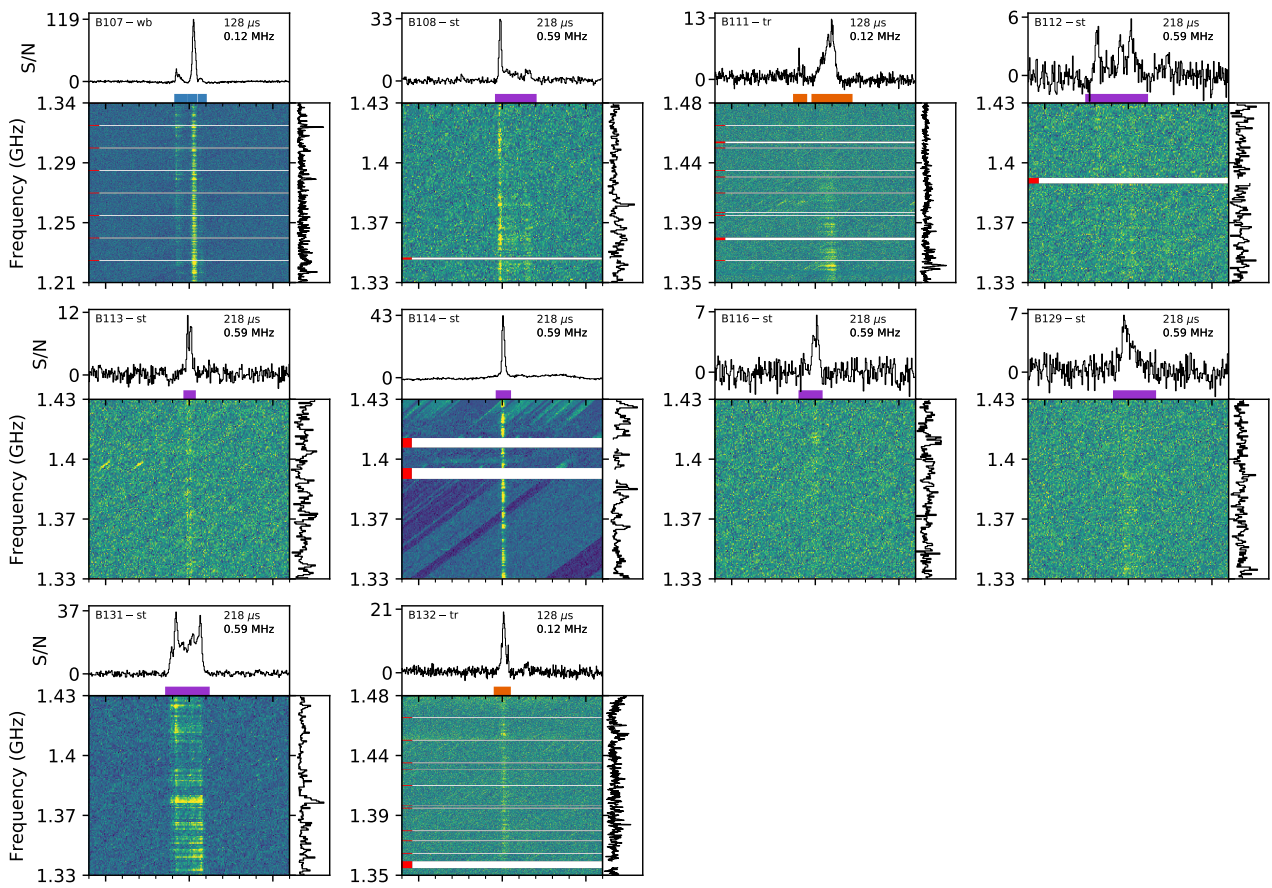
Supplementary Data Figure 1 (Cont.)



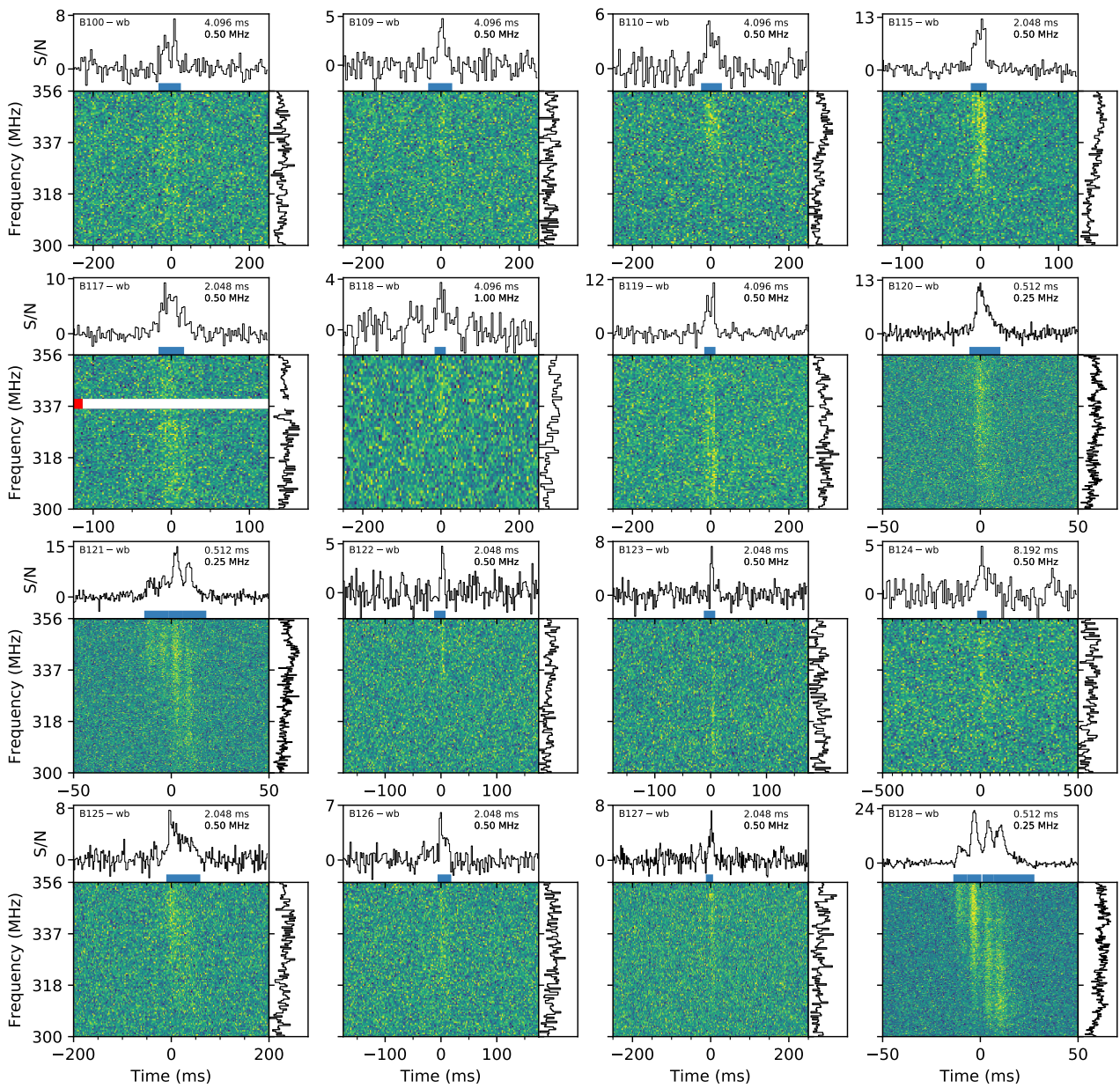
Supplementary Data Figure 1 (Cont.)



Supplementary Data Figure 1 (Cont.)



Supplementary Data Figure 1 (Cont.)



Supplementary Data Figure 1 (Cont.)